# Extensive topographic remapping and functional sharpening in the adult rat visual pathway upon first visual experience

Joana Carvalho*, Francisca F. Fernandes and Noam Shemesh*

*Laboratory of Preclinical MRI, Champalimaud Research, Champalimaud Centre for the Unknown, Lisbon, Portugal*

*Corresponding authors:

Dr. Noam Shemesh, Champalimaud Research, Champalimaud Foundation, Av. Brasilia 1400-038, Lisbon, Portugal E-mail: Noam.Shemesh@neuro.fchampalimaud.org
Phone number: +351 210 480 000 ext. #4467; ORCID: 0000-0001-6681-5876
Dr. Joana Carvalho, Champalimaud Research, Champalimaud Foundation, Av. Brasilia 1400-038, Lisbon, Portugal E-mail: Joana.Carvalho@research.fchampalimaud.org
Phone number: +351 210 480 000 ext. #4467; ORCID: 0000-0002-0081-1976

**Author Contributions:** JC and NS wrote the manuscript; JC conceived the idea; NS supervised the research; JC collected the data, JC and FFF performed the data analysis; all authors reviewed the manuscript.

**Acknowledgement:** We would like to thank Rita Gil and Federico Severo for setting up the Visual deprivation room. This study was funded by the European Research Council (ERC) (agreement No. 679058), as well as by the European Union's Horizon 2020 research and innovation programme under the Marie Sklodowska-Curie grant agreement No. 101032056. The funding organization had no role in the design, conduct, analysis, or publication of this research. The authors acknowledge the vivarium of the Champalimaud Centre for the Unknown, a facility of CONGENTO which is a research infrastructure co-financed by Lisboa Regional Operational Programme (Lisboa 2020), under the PORTUGAL 2020 Partnership Agreement through the European Regional Development Fund (ERDF) and Fundação para a Ciência e Tecnologia (Portugal), project LISBOA-01-0145-FEDER-022170.

**Competing Interest Statement:** None

**Keywords:** Plasticity, high field fMRI, visual field mapping, receptive field, computational modeling, visual deprivation

# Abstract

Understanding the dynamics of stability/plasticity balances during adulthood and how they are sculpted by sensory experience is pivotal for learning, disease, and recovery from injury. Although invasive recordings suggest that sensory experience promotes single-cell and population-level plasticity in adults, the brain-wide topography of sensory remapping remains unknown. Here, we investigated topographic remapping in the adult rodent visual pathway using functional MRI (fMRI) coupled with a first-of-its-kind setup for delivering patterned visual stimuli in the scanner. Using this novel setup, and coupled with biologically-inspired computational models, we were able to noninvasively map brain-wide properties (receptive fields (RFs) and spatial frequency (SF) tuning curves) that were insofar only available from invasive electrophysiology or optical imaging. We then tracked the RF dynamics in the chronic Visual Deprivation Model (VDM), and found that light exposure progressively promoted a large-scale topographic remapping in adults. Upon light exposure, the initially unspecialized visual pathway progressively evidenced sharpened RFs (smaller and more spatially selective) and enhanced bandpass filters in SF tuning curves. Our findings reveal that visual experience following VDM reshapes the structure and function of the visual system and shifts the stability/plasticity balance in adults.

# 1. Introduction

During critical periods of development, neural circuits undergo massive plasticity and organization processes that are strongly shaped by sensory experience (Dunn et al. 2013; Eimer 2004; Hooks and Chen 2007; Kalia et al. 2014). At later stages of life, these plastic changes must reach a certain degree of stability, to ensure that the gained functional refinements persist over time. Understanding the dynamics of stability/plasticity balances and how they are sculpted by experience is pivotal both for identifying mechanisms underlying normal/aberrant development and for recovery from injury.

Most studies demonstrating plasticity in rodents have focused on local features. For example, seminal electrophysiological and calcium recordings studies revealed that activity in specific junctions of the rodent visual pathway becomes highly refined during the first ~4-5 weeks of life (Teller et al. 1978; Wiesel and Hubel 1963; Fagiolini et al. 1994). The initially broadly-tuned cortical neurons specialize towards well-defined functional properties, i.e sharper spatial frequency (SF) tuning, and an orderly cortical arrangement of visual areas emerges such that neighboring neurons respond to nearby positions in the visual field (retinotopic organization) (Tschetter et al. 2018; Koehler, Akimov, and Rentería 2011; Hubel and Wiesel 1962). Visual experience refines immature Receptive Fields (RFs) and the underlying neural connectivity, initially established by spontaneous activity, to improve their selectivity (Morales, Choi, and Kirkwood 2002; Mower and Christen 1985; Jenks and Shepherd 2020; Huberman, Feller, and Chapman 2008). As the critical period ends, the plastic potential of the brain decreases and gradually reaches a stable state to support network stability (Fagiolini et al., 1994; Fagiolini and Hensch, 2000; Gordon and Stryker, 1996).

Despite the importance of plasticity for e.g. disease and recovery from injury in adulthood, whether a large-scale topographic remapping could be achieved during adulthood remains an open and controversial question. For example, in the Visual Deprivation Model (VDM), (Mower 1991; Fagiolini et al. 1994; Iwai et al. 2003; Hubel and Wiesel 1970), where animals are reared in complete darkness from birth and before exposure to light, the system is in an aberrant state on multiple scales. From a cellular perspective, RFs do not exhibit the sharp properties of normal rodents, and cortical function and structure resemble the conditions typically observed before eye opening. In particular, broad spatial and SF tuning selectivity, (Fagiolini et al. 1994; Sherman and Spear 1982; Gianfranceschi et al. 2003) are found. Furthermore, at the population level, a lack of orderly visual maps and imprecise RF tuning (Jenks and Shepherd 2020; Smith and Trachtenberg 2010) was found. Behaviourally, visual acuity remains low (Regal et al. 1976; Teller et al. 1978; Timney, Mitchell, and Giffin 1978).

Exposure to light following VDM provides an outstanding opportunity to investigate plasticity/stability balances in adulthood. Whether first light exposure in adulthood promotes a normal development of the visual system is highly controversial, with some electrophysiology studies suggesting that VDM results in permanent deficits most likely driven by aberrant excitatory–inhibitory balances (Di Marco et al. 2009; Gianfranceschi et al. 2003), supporting the view of a remarkable degree of stability in the adult visual system (Daw et al. 1992; Hubel and Wiesel 1970; T. K. Hensch et al. 1998; Baseler et al. 2011). Others however, support the view that the brain remains plastic after the critical period by cortical remapping, in particular, through re-scaling and displacing RFs, in response to visual deprivation (Womelsdorf et al. 2006; Kaas et al. 1990; Keck et al. 2008, 2011; Hübener and Bonhoeffer 2014). These findings are corroborated also by lesion studies (Womelsdorf et al. 2006; Kaas et al. 1990; Keck et al. 2008, 2011; Hübener

and Bonhoeffer 2014). In particular, although the studies above provide some evidence that a reorganization occurs upon first light exposure in adulthood, it is still unclear whether the system itself exhibits a convergence to the normal topographical mapping and whether it does so in unison or whether different areas of the brain have distinct dynamics. This gap stems from the macroscopic nature of entire networks and the inherently multidimensional time scales involved.

Insofar measurements of RF properties in rodents has been limited to electrophysiological measurements of few sparsely distributed neurons (Kaas et al. 1990; Keck et al. 2008; Fagiolini et al. 1994) and by calcium imaging (Zhuang et al. 2017) focusing only on isolated brain regions, lacking the pathway-wide perspective (Girman, Sauvé, and Lund 1999; Meliza and Dan 2006). Furthermore, RF properties are typically compared pre- and post- lesion/conditioning (Kaas et al. 1990; Keck et al. 2008; Meliza and Dan 2006). The difficulty of monitoring the same cells (e.g. via electrophysiology or calcium imaging) at different time points may lead to neuronal changes unrelated to plasticity. These bottlenecks limit our knowledge on how the entire pathway adapts and generates a specialization of detailed RFs and SF, which is critical for developing future therapies and rehabilitation strategies.

Here, to enable the investigation of entire-pathway plasticity, we bridge this critical gap using preclinical high field functional Magnetic Resonance Imaging (fMRI) coupled with a novel setup capable of delivering complex visual stimuli in the scanner (Figure 1). MRI provides the required whole-pathway view and longitudinal capacity, and population receptive fields (pRF) properties are routinely measured non-invasively in humans and non-human primates, although at a coarse level of detail (Dumoulin and Wandell 2008; Wandell, Dumoulin, and Brewer 2007). In addition, high-field preclinical MRI has proven ability to map in a highly detailed manner brain wide plasticity (Dijkhuizen et al. 1996; Hoehn et al. 2001) after sensory deprivation (Yu et al.

2010; Gil, Fernandes, and Shemesh 2021), peripheral nerve injury (Pelled et al. 2007; Yu et al. 2012), and stroke (M.-Z. Li et al. 2018; Alves et al. 2021). However, delivery of such complex stimuli for rodents, which would enable a broad spectrum of experiments that are not possible to perform in human or primate counterparts, was insofar considered "impossible" due to space constraints in preclinical scanners. Using this first-of-its-kind setup, we mapped in detail the topographical and neuroanatomical organization of the entire rodent visual pathway for the first time, thereby linking the population level RFs vis-a-vis electrophysiology, of entire visual areas at a whole pathway-level and in a non-invasive manner. We could then probe the plasticity/stability balance in an animal model where control can be exerted on the visual landscape and rearing conditions, i.e adult rodents using the VDM, and follow if and how the system specializes in terms of RFs and SF tuning curves. Our results suggest that light exposure in adulthood results in an extensive topographical remapping and functional sharpening. The outcomes of this study have important implications for visual rehabilitation and restoration therapies.

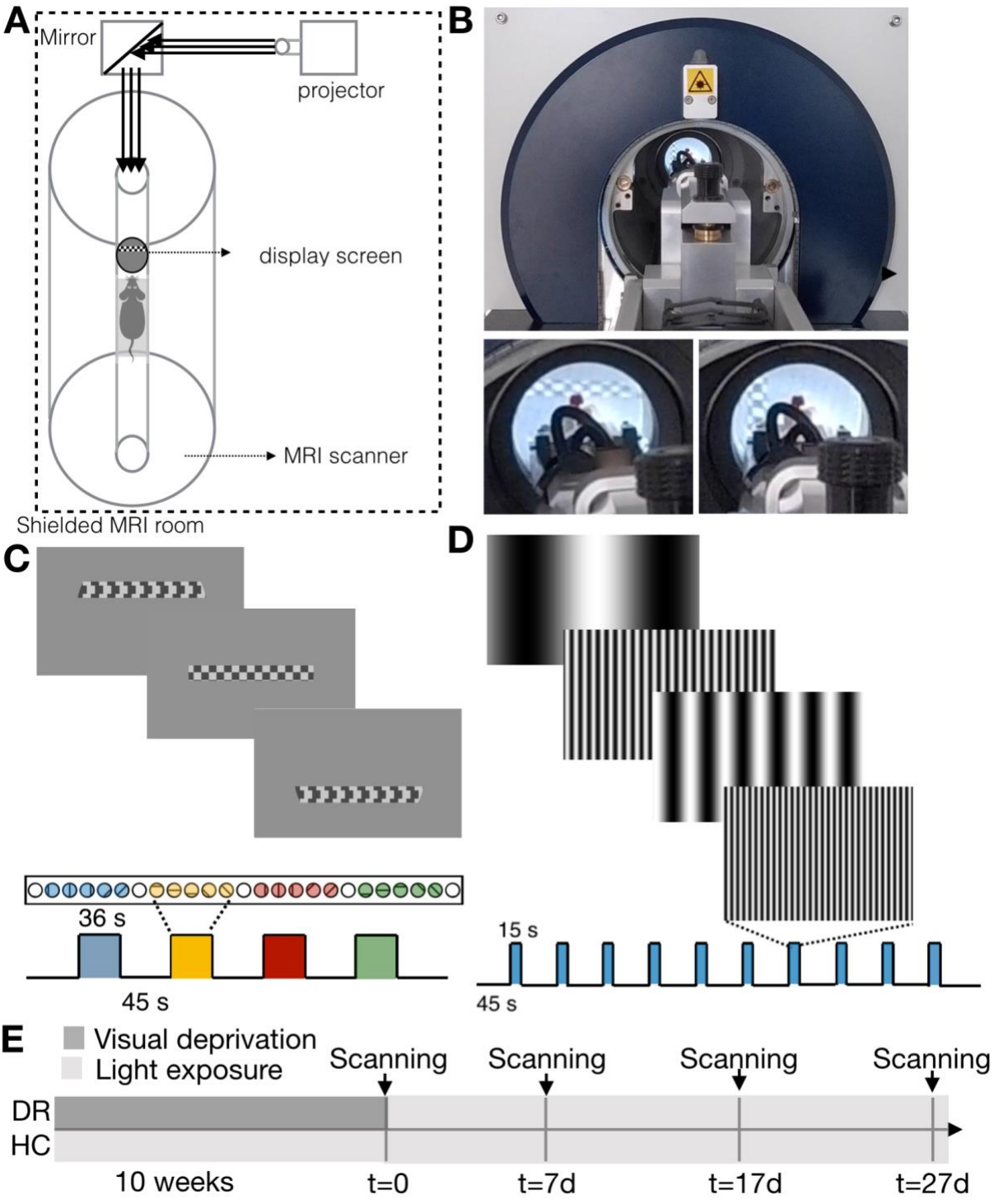


**Figure 1. The complex visual stimuli setup for preclinical MRI scanners, stimulation paradigms and scheme of the dark rearing timeline.** A: Visual stimulus display setup. B: Picture of the visual stimulus displayed inside the scanner. C: The retinotopy stimulation paradigm: checkerboard bar moving in 8 different directions (2 directions per stimulation block during 36 s followed by a 45 s rest period, repeated 4 times). D: The SF tuning paradigm: 15 s stimulation period followed by a 45 s baseline. Ten different SFs were randomly presented at each stimulation block ranging between 0.003 and 0.5 cpd. E: Timeline of the dark rearing experiment.

# 2. Results

## 2.1 Retinotopic organization of the rat visual pathway mapped via fMRI

Figures S1, S2 and 4 show that the complex visual stimuli setup elicited reliable, temporally reproducible, and robust BOLD activation throughout the entire visual pathway in response to both retinotopic and SF tuning stimuli.

To validate the relevance of the complex visual stimulus setup, we first set to perform retinotopy in the rat using fMRI. The RF properties of the population of neurons within each voxel - referred to as "population RF" (pRF) (Dumoulin and Wandell 2008) - were mapped voxelwise. Each pRF was modeled by a 2D Gaussian model and therefore characterized by a center (eccentricity and polar angle-phase) and a size. In addition, we mapped the pRF profiles, which capture the visual representation of each pRF through visual field sampling using very small (0.01º) probes (Carvalho et al. 2020). Figure 2A shows retinotopic (phase) maps averaged across animals for three representative slices containing the main junctions of the visual pathway, namely, lateral geniculate nucleus (LGN), superior colliculus (SC) and visual cortex (VC) areas. For all the studied areas, clear retinotopic organization was evidenced, and neighboring voxels responded to adjacent positions in the visual field as expected. Note that the visual information crosses at the optic chiasm, so the pRFs in the left hemisphere respond to the visual information presented on the right part of the visual field, and vice-versa (Figure 2B). In VC, the phase variation occurs along each cortical layer and it does not appear to vary across cortical depth. In the SC and LGN, strongly organized retinotopic maps were also observed.

The visual field representation for a determined ROI can be reconstructed by: 1) converting the pRF profiles into heat maps (histograms of a 30 × 30 bin grid weighted by its bin variance

explained) and 2) aggregating the RFs across the voxels in an entire ROI via a normalized sum (Carvalho et al. 2021). Figure 2C shows the visual field reconstruction at the level of VC, corresponding to what the animal is actually seeing. The yellow regions of the visual field were more highly sampled by the VC during the retinotopic paradigm. The overlap between VC visual field reconstruction and the available FOV is evident and, due to animal bed constraints, corresponds only to the top half of the visual field.

Using our setup, we could also determine the size of the receptive fields. In the VC, RF size changes across cortical layers and is constant within layers (Figure 2D), as expected. Figure 2E shows how pRF sizes vary with cortical depth. While superficial and deeper layers present larger pRFs, layer IV contains the smallest pRFs (Figure 2E). This is also clearly depicted in the pRF profiles across cortical layers (Figure 2F). These findings are in line with electrophysiological studies in cats and human fMRI reports, where the smallest RF sizes are found in layer IV and the largest at layer VI (Fracasso, Petridou, and Dumoulin 2016; Gilbert 1977). The uncertainty associated with the pRF size estimates increases with cortical depth, likely due to the depth profile of our surface coil and the choice of coronal slices, which impart more partial volume effects in the slice direction.

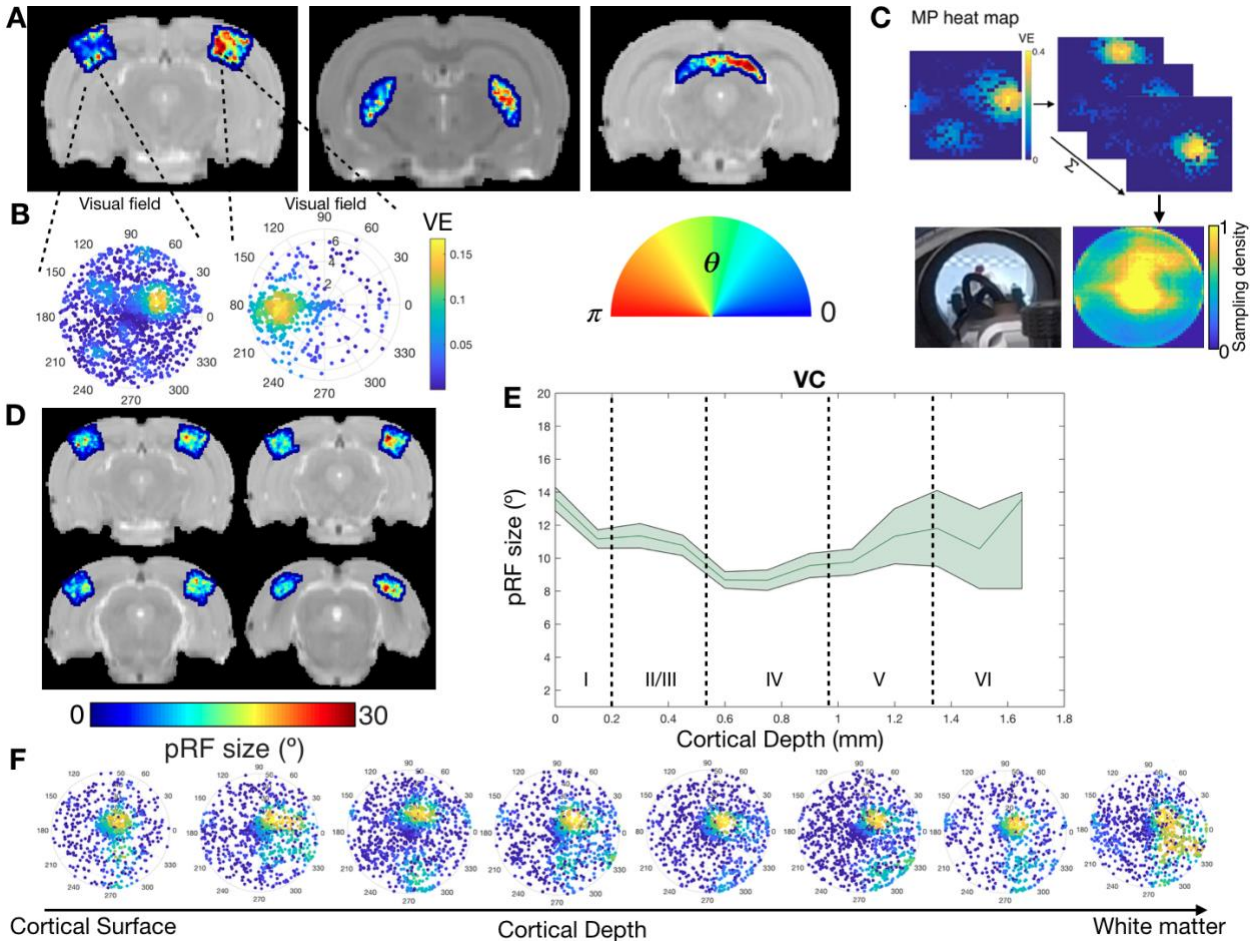


**Figure 2. PRF estimates of HC animals across ROIs and cortical layers at t=0.** A: Phase maps averaged across animals obtained for VC, LGN and SC, respectively. The colorbar shows the preferred angle estimated per each voxel. B: Visual representation of two pRF profiles located in the left and right hemispheres, respectively. The colorbar shows the variance explained (VE) of each individual probe. C: Average visual field reconstruction maps across animals for VC (obtained by summing the RF maps across some voxels of VC) and an image of the visual setup depicting the portion of the FOV covered by the animal bed. D: RF size maps averaged across animals in four different slices of the VC. The colorbar corresponds to degree of visual angle. E: Profile of the RF size across cortical depth averaged across subjects, obtained from two slices of the VC. The green area corresponds to the 10% confidence interval. F: Visual representation of eight pRF profiles located across layers of the VC.

## 2.2 Spatial frequency selectivity across the rat visual pathway mapped via fMRI

Spatial frequency selectivity is another core characteristic of the mammalian visual system, and its whole-pathway features in rodents have never been measured. Here, we measured SF selectivity across multiple structures of the rat visual pathway and derived their specific SF tuning curves

(Figure 3). Figure 3A shows the definition of the ROIs (LGN, SC and VC) according to the Paxinos and Watson rat brain atlas overlaid on top of the anatomical images of a particular HC animal. The projection of the optimal SF per voxel is shown in Figure 3B. In contrast with the retinotopic maps, within each visual structure (ROI), we find no organization of SF selectivity, which indicates that each area responds globally to a set of specific SFs. Figure 3C shows the SF tuning curves in LGN, SC and VC in HC. Overall, all the ROIs show a band-pass filter tuned to low SF behavior. Early areas of visual processing such as SC have lower optimal SF than areas that process visual information at a later stage in the visual hierarchy, such as VC. The variation in SF across visual areas is most likely associated with the different filtering behaviors that diverse neurons exhibit, i.e. some neurons present a low-pass filter behavior while others exhibit a band-pass (Sriram, Meier, and Reinagel 2016). The average optimal SF estimated for VC, LGN and SC of HC animals is 0.12 cycles per degree (cpd), 0.06 cpd and 0.05 cpd, respectively. The optimal SF values are in agreement with what has been reported in the literature through calcium and electrophysiology: neurons in the LGN region of awake rats best respond to SFs of 0.03-0.06 cpd (Sriram, Meier, and Reinagel 2016); neurons in VC have a peak response at 1 cpd (Girman, Sauvé, and Lund 1999); and neurons in SC show band-pass profiles with an optimal SF of 0.03 cpd and large tuning widths (Prévost, Lepore, and Guillemot 2007). These reference values are highlighted in Figure 3C.

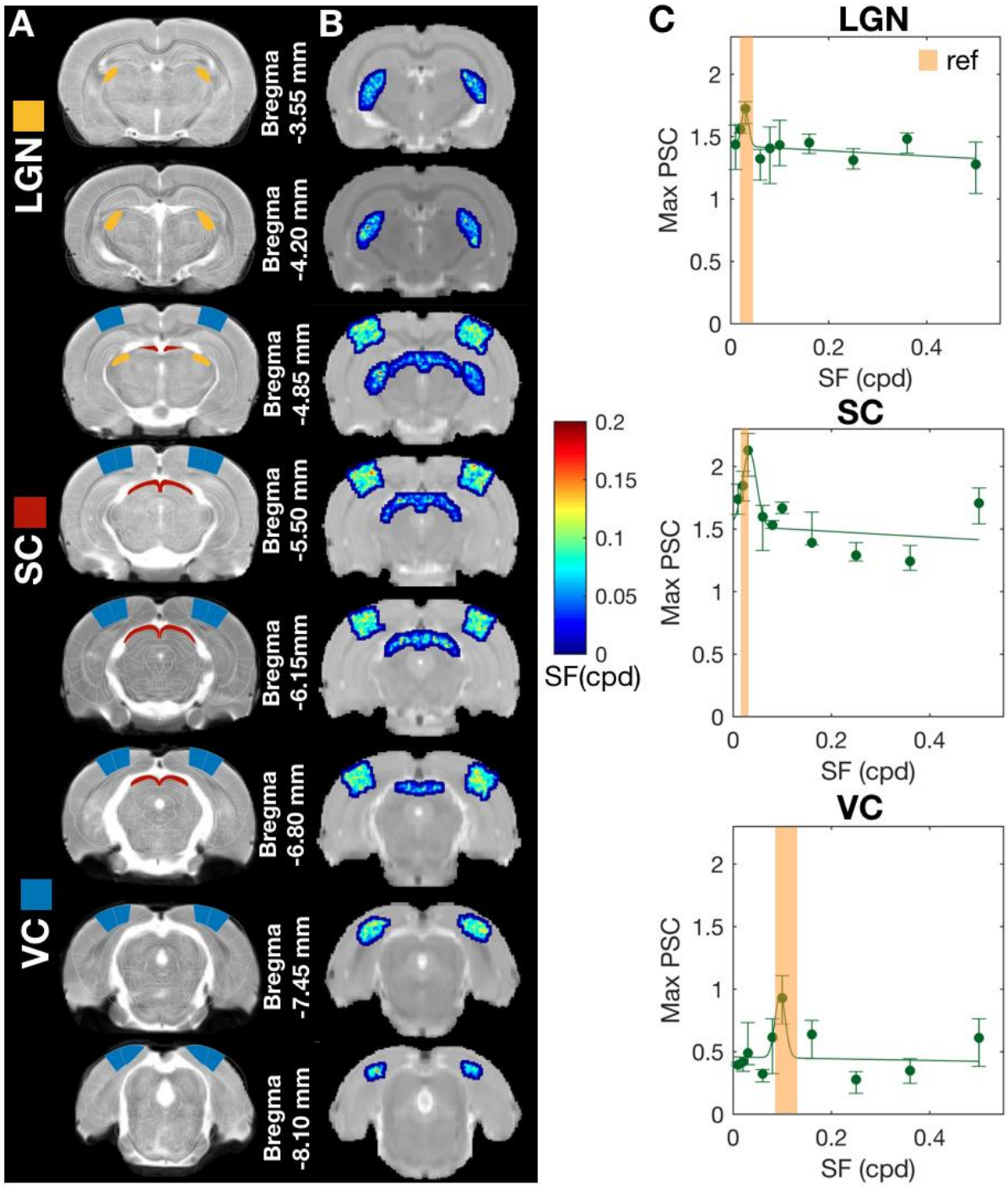


**Figure 3. Spatial frequency selectivity across the visual pathway in HC animals at t=0.** A: Anatomical images with Paxinos and Watson Atlas structures overlaid and the ROIs highlighted. B: Optimal SF estimated per voxel for HC, averaged across animals. C: Maximum PSC during the activation period as a function of the SF of the stimulus, calculated for HC. The errorbar represents the 10% confidence interval across animals. The continuous lines represent the Gaussian model fitted to the data. The goodness of fit is shown in Table S1. The orange band denotes the range of optimal SF values reported in the literature measured using electrophysiology (Sriram, Meier, and Reinagel 2016).

## 2.3 Visual deprivation results in differential BOLD dynamics throughout the visual pathway

Once we verified that the complex stimuli setup provides insight into the visual pathway organization, we sought to probe the plasticity/stability balance in the adult brain. We first evaluated global fMRI responses in the VC, LGN and SC of mice that underwent visual deprivation (Dark Reared (DR)) as a model of plasticity and compared them to activity in healthy controls (HC) in terms of retinotopic and spatial frequency characteristics at multiple time points (t = 0, t = 7d, t = 17d and t = 27d, Figures 4 and S2, respectively).

Upon first exposure to light in animals DR from birth, the fMRI responses to the retinotopy stimulus at this t=0 were characterized by a markedly faster onset in the DR group when compared with HC in VC and LGN. In the first 10 s of visual stimulation, the BOLD response in VC and LGN in the DR group was significantly higher than in HC (Figure 4C and 4D). In the VC in particular, stronger differences between the DR and HC were observed in response to the SF tuning stimulus (Figure S2). The DR group BOLD responses to the SF tuning stimulus exhibited 3-fold increases in BOLD amplitudes in VC compared to HC at t = 0 ($p$-value<0.001, Figure S2). Interestingly, one week after light exposure, the DR BOLD responses in the VC were attenuated to the level of the HC for both retinotopic and SF tuning stimuli. At t = 7d, t = 17d and t = 27d, there were no significant differences between the amplitude of the VC BOLD responses of DR and HC animals (Figure 4E-M and Figure S2).

Moreover, the HCs show stronger signals in the LGN during the entire stimulation period in response to the retinotopic stimulus at t = 0, t = 17d and t = 27d (Figure 4 D, J and M, respectively). Interestingly, the most striking difference between the responses to both stimuli

takes place in the SC. For all time points, the DR SC exhibited a negative BOLD response to the retinotopic stimulus, contrasting with the positive BOLD response measured in HC. This difference was highly statistically significant in all time points (Figure 4D, G, J and M). This contrasts with the responses obtained in SC to the SF tuning stimulus, where the DR BOLD response is positive at all time points and even shows increased values compared to the HC at t = 27d (Figure S2).

To summarize, visual deprivation: a) boosts BOLD-fMRI responses and results in faster onset times in the visual cortex; and b) results in negative BOLD responses in the SC in response to the retinotopic stimulus. Moreover following light exposure the responses in the VC of DR animals are comparable to the ones of HC and remain attenuated in the SC and LGN.

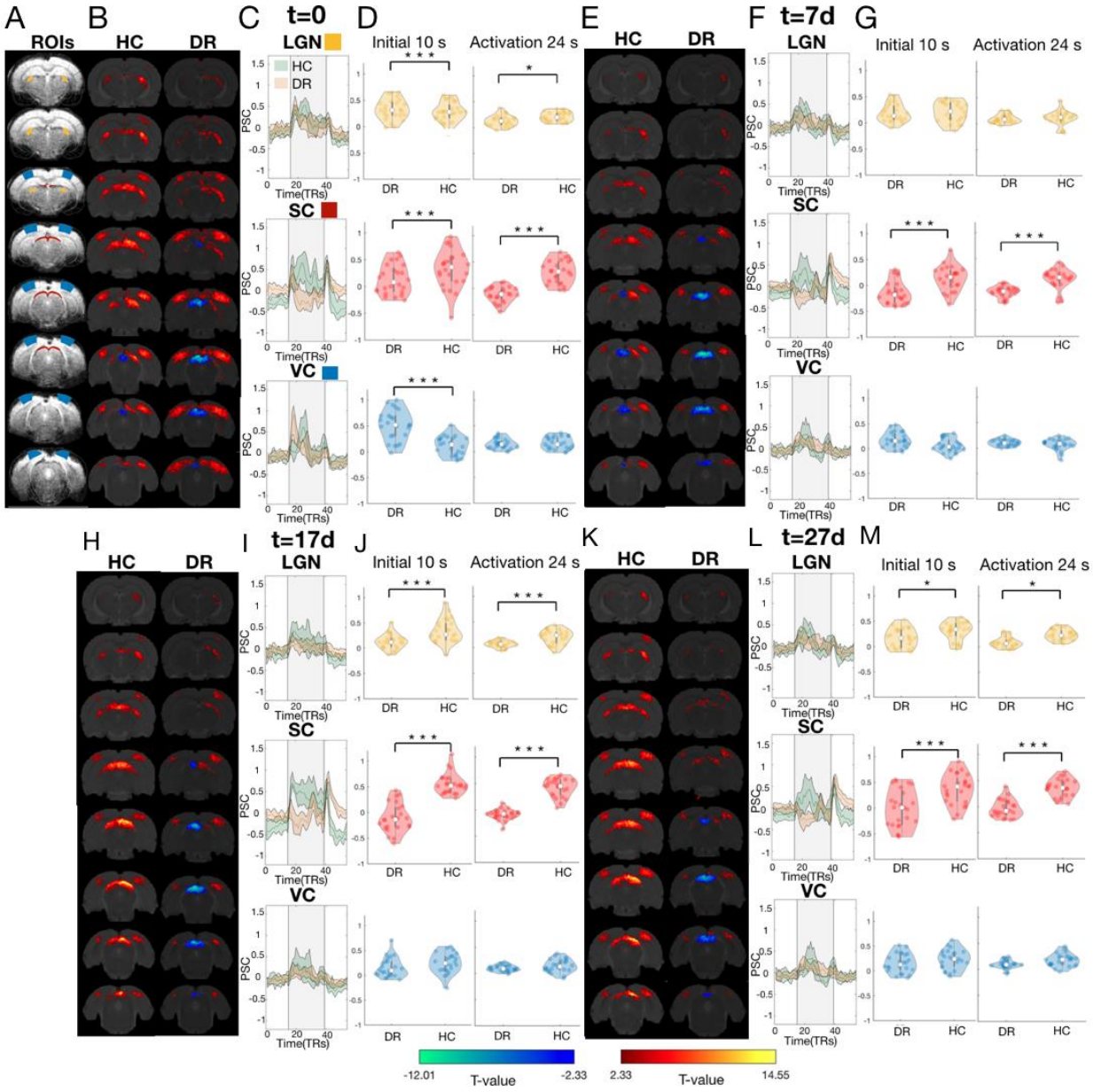


**Figure 4. Differential responses between DR animals and HC driven by the retinotopic stimulus.** A: Raw fMRI images with the ROIs (LGN, SC and VC) overlaid. B, E, H, K: fMRI activation patterns of t-contrast maps obtained for HC and DR animals at t=0, t=7d, t=17d and t=27d, respectively. The GLM maps are FDR corrected using a p-value of 0.001 and minimum cluster size of 20 voxels. C, F, I, L: PSC of the LGN, SC and VC for the HC and DR animals at t=0, t=7d, t=17d and t=27d, respectively. The grey area represents the stimulation period. D,G, J, M: Violin plot of the amplitude of the BOLD response of DR and HC during the initial 10 s of the activation period (left) and the total duration of the activation period obtained with the retinotopy stimulus (right) at t=0, t=7d, t=17d and t=27d, respectively. The white dot represents the mean, and the grey bar represents the 25% and 75% percentiles. The blue, yellow and red colors represent the VC, LGN and SC respectively. The *** represents a p-value<0.001, ** p-value<0.01 and * p-value<0.05.

## 2.4 Large-scale and pathway-wide topographical remapping in adulthood following visual deprivation

To gain more specific insights into the reorganization of the adult visual pathway in the brain, we longitudinally tracked changes in pRFs position and size for HC and DR. Figure 5A shows the average phase maps across HC and DR animals obtained for VC, LGN and SC, respectively. At t = 0 it is evident that while the HC group displays clear retinotopic organization, the DR topography is highly disorganized.

Interestingly, after first light exposure in the adult DR group, the visual pathways progressively become retinotopically organized, and start to resemble the retinotopic organization observed in HC. This progressive organization is particularly apparent in SC (Figure 5). To further quantify this effect we computed the difference of the pRF estimated position between each ROI's voxels as a function of the distance between each pair of voxels across the four time points tested. At t = 0, for all the ROIs, the DR animals show a larger difference between the pRF position estimates than HC. This difference is larger for neighboring voxels and it becomes less pronounced for larger distances between voxels. Across scanning sessions the variation in estimated pRF position of the DR becomes closer to the one of HC. The DR's average correlation across ROIs between pRF position variation and the voxel's distance increases across the scanning sessions and at t = 27d it is at the level of HC (DR: t = 0, $r^2 = 0.53$; t = 7d, $r^2 = 0.61$; t = 17d, $r^2 = 0.76$; t = 27d, $r^2 = 0.85$; HC: t = 0, $r^2 = 0.77$; t = 7d, $r^2 = 0.76$; t = 17d, $r^2 = 0.78$; t = 27d, $r^2 = 0.84$, all p-values<0.001, all the correlation values are presented in Tables S1 and S2). Only SC does not recover completely to HC levels after 27d, as noted by both qualitatively assessing the maps and the differences in the red and blue curves (Figure 5).

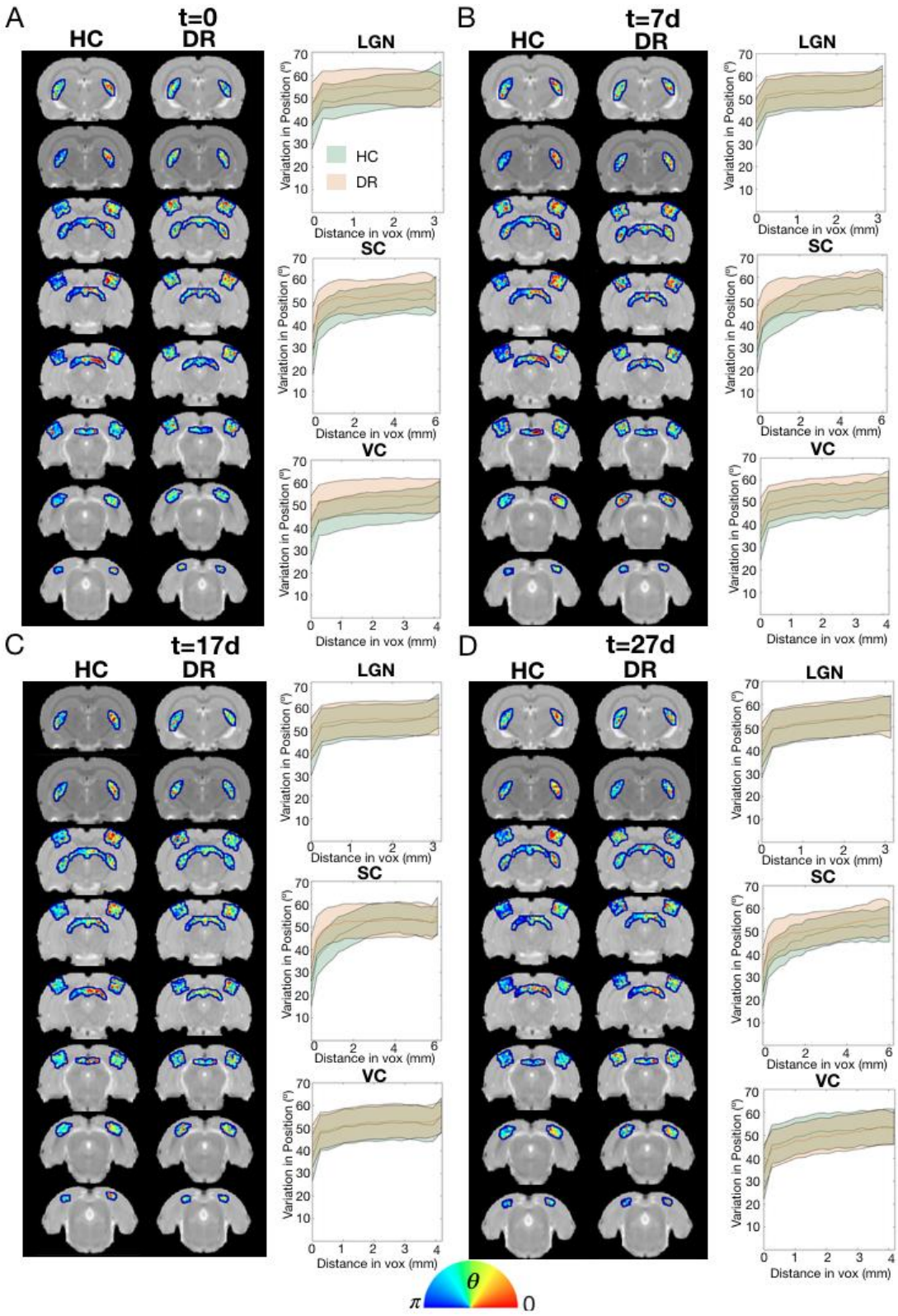


**Figure 5. Refinement of RF position across time for DR and HC.** A: Average phase maps obtained for 8 different slices and graphs showing the variation in pRF position measured between voxels of the same ROI as a function of the Dijstra's distance between voxels, both obtained for DR and HC at the 4 measured time points. The solid lines represent the mean and standard deviation (std).

Next we investigated whether the progressive organization of the visual pathways is accompanied by a decrease in pRF size. Figure 6A shows the average pRF size across animals and ROIs for HC and DR at the different time points. At t = 0 the pRF size in VC and SC is significantly larger in DR than in HC. One week after light exposure the DR's pRFs in VC, LGN and SC pRF size are significantly smaller compared to its values at t=0. For VC and SC at t=7d the DR's pRF values were at the level of HC. In LGN DR's pRF size gradually shrinks across scanning sessions, in addition the pRF size in HC was larger than in DR at all the time points measured, this effect becomes significant at t = 27d. Importantly the HC pRF estimates for VC, LGN and SC did not significantly differ between scanning sessions. Furthermore the averaged pRF size estimated per visual area in HC (VC = 15º; LGN = 18º; SC = 12º) are in line with values reported in the literature and they are in agreement with the size expected taking into account the hierarchy of the visual pathway (Dräger 1975; Binns and Salt 1997). Note our model assumes simple on-center RFs. This provides further evidence of reliability of the pRF estimates. Figure 6B shows the variation in pRF size across cortical layers for HC and DR at multiple scanning sessions. The reduction of RF sizes took place mostly in the superficial and middle layers. At t = 0 the pRF sizes at the deepest layers do not differ significantly between HC and DR. Furthermore at t = 0 the variation of the pRF size across cortical layers does not follow the trend of the HC, in the DR the pRF size continuously decreases from the cortical surface until the deepest layer. Figure 6C shows RF profiles of two VC voxels, one of HC5 and another of DR5 across scanning sessions; we can appreciate how the DR pRF becomes more refined over scanning sessions.

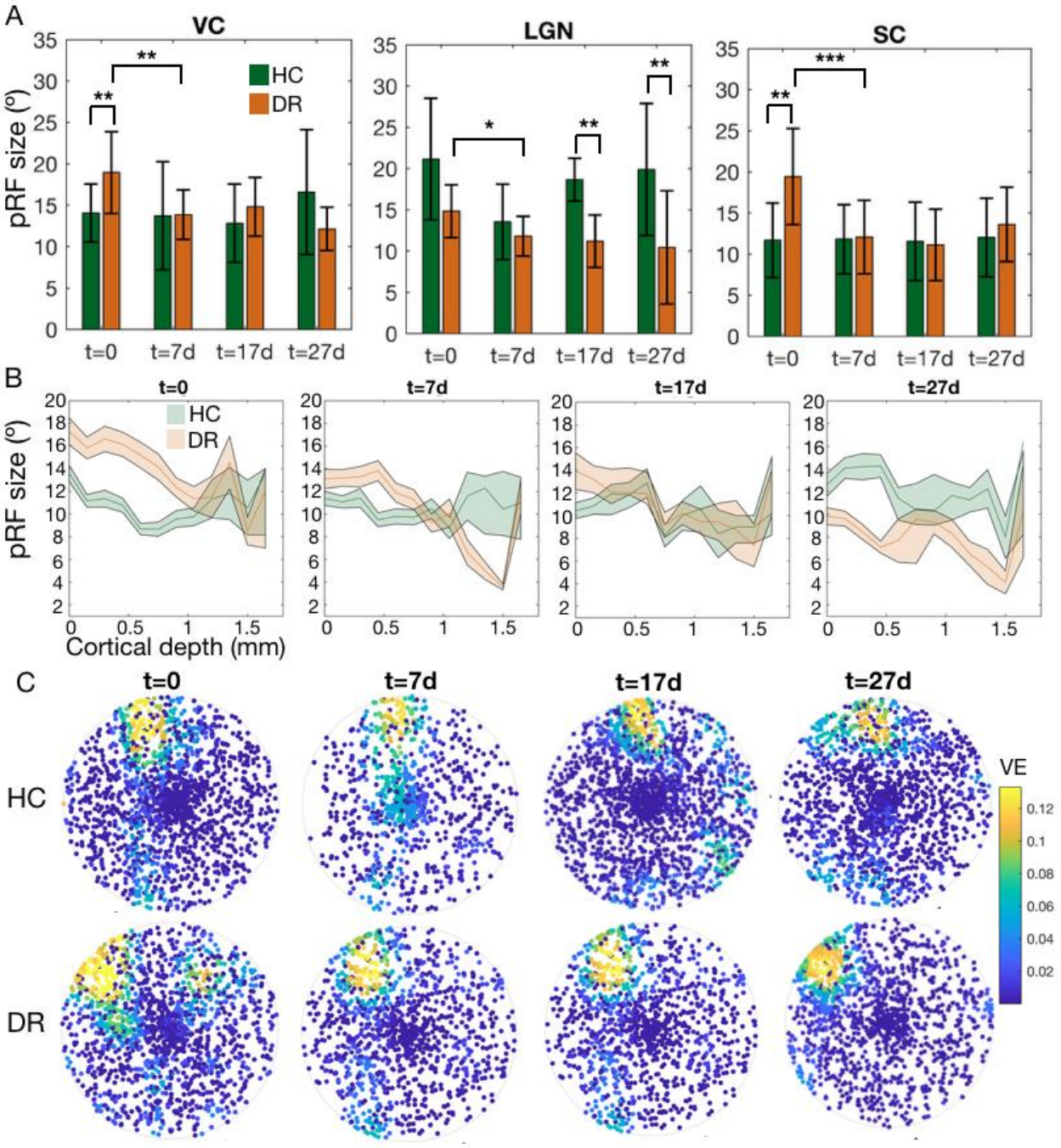


**Figure 6. Refinement of RF size across time for DR and HC.** A: Average RF size measured for HC and DR at multiple time points for VC, LGN and SC. The errorbar corresponds to std. The *** represents a p-value<0.001, ** p-value<0.01 and * p-value<0.05. B: Variation of the RF size averaged across animals as a function of the cortical depth for two slices of the VC for DR and HC at multiple time points. C: Visual representation of two population RF profiles (one in HC and another in DR) across the 4 scanning sessions.

## 2.5 Specialization of spatial frequency selectivity is promoted by visual experience

A hallmark sign of specialization of the visual pathway is the refinement of tuning curves (Hoy and Niell 2015). Figure 7A shows the projection of the optimal SF obtained per voxel. At t=0 a wider range of SFs are apparent for the DR group VC, LGN and SC when compared to the same structures in HCs, while at t = 7d, the DR maps are more similar to HC's. Figure 7B represents the SF tuning curves in VC, LGN and SC at the four time points tested. Panel 7C shows how the optimal SF (Gaussian center) and broadness of the tuning curves (Gaussian width) are shaped by visual experience in HC and DR. For all the visual structures tested (VC, LGN and SC) at t = 0 the DR tuning curves are broader than HC ones (VC $t(39)=-2.48$ p-value<0.01, LGN $t(39)=-3.7$ p-value<0.001; SC $t(39)=-2.61$ p-value<0.01); panel C. At t = 7d the DR SF tuning curves become similar to HCs, narrower and with an aligned peak (optimal SF frequency). Note the drop in optimal SF and SF tuning curve with from t = 0 to t = 7d in panel 7C. This is particularly evident in the LGN which shows a much higher correlation between the DR and HC tuning curve points at t = 7d than at t = 0, (t = 0 $r^2=0.11$, t = 7d $r^2=0.73$). While at t = 17d and t = 27d the values of optimal SF estimated for DR tend to stabilize near the SF values estimated for HC, the broadness of the tuning curve is more variable. After the initial shrinkage in SF tuning broadness from t = 0 to t = 17d, at t = 27d LGN and SC show large tuning curves, panels 7B and 7C. With the exception of LGN where the HC's SF curves become larger over time and the optimal SF is shifted toward higher values, the optimal SF and broadness of the tuning curve estimated for VC and SC for HC do not vary significantly between time points. In addition areas with strong BOLD signals such as SC the SF estimates tend to be less variable.

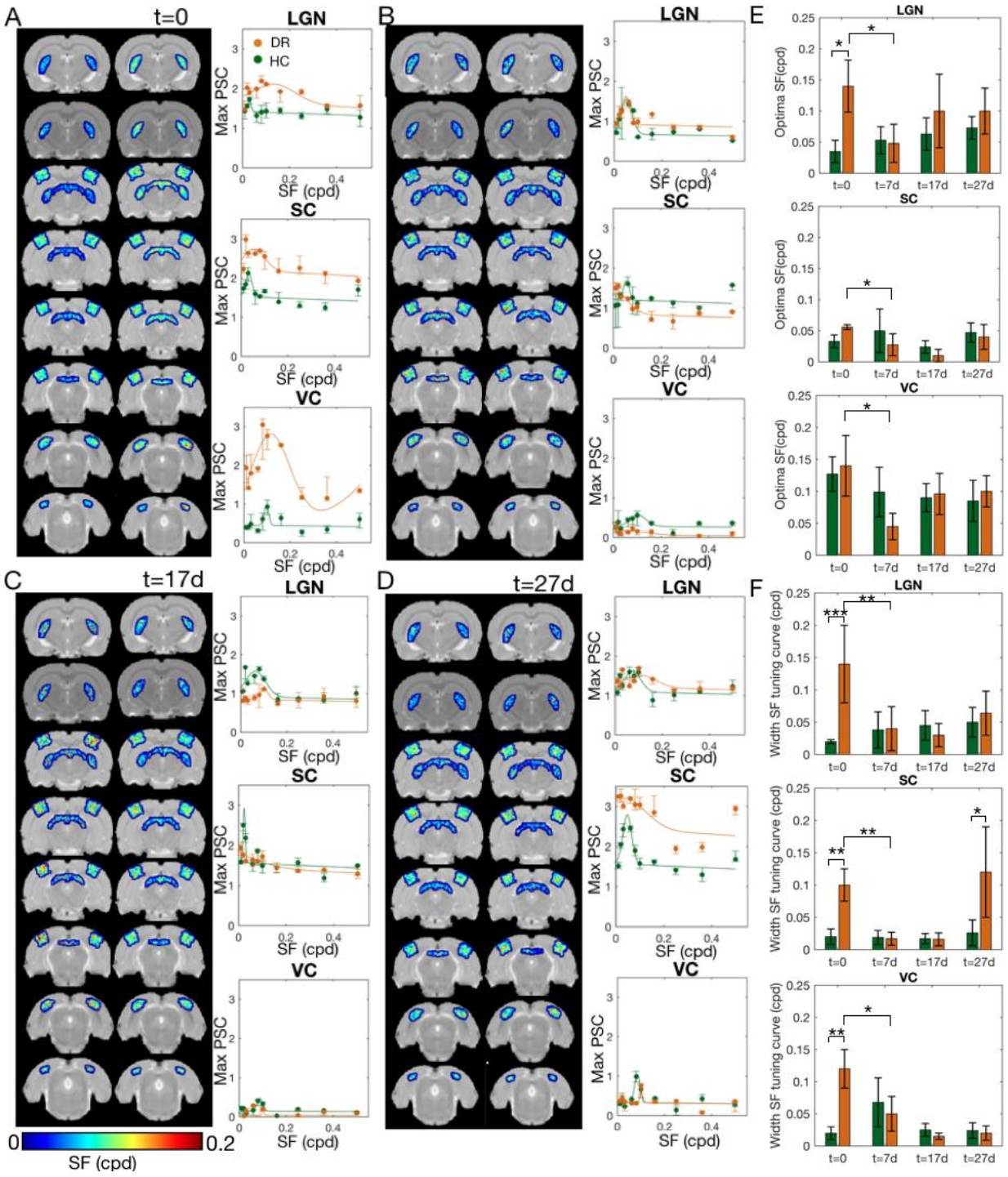


**Figure 7. Visual experience following VDM promotes the specialization of SF tuning curves.** A, B, C, D: Optimal SF estimated per voxel for HC and DR, at t=0, t=7d, t=17d and t=27d respectively. E: Maximum PSC during the activation period as a function of the SF of the stimulus, calculated for DR (orange) and HC (green) at the four measured time points. The errorbar represents the std. The continuous lines represent the Gaussian model fitted to the data. F: Estimated optimal SF (Gaussian center) and broadness of the SF tuning curve (Gaussian width) for the VC, LGN and SC at t=0, t=7d, t=17d and t=27d for HC and DR. The errorbar corresponds to std. The *** represents a p-value<0.001, ** p-value<0.01 and * p-value<0.05.

# 3. Discussion

The unique setup for delivery of complex stimuli in rodent preclinical fMRI scanners developed here enabled an in-depth investigation of the plasticity/stability balance in the adult visual pathway. Delivery of such complex stimuli enabled the first fMRI-based mapping of retinotopic organization and SF tuning of the visual pathway in adult rats. In healthy controls, the estimation of the RF properties via BOLD-fMRI reproduced at a pathway-level all the trends expected from prior invasive calcium recording and electrophysiology studies (Zhuang et al. 2017; Espinoza and Thomas 1983; Girman, Sauvé, and Lund 1999; X. Li, Sun, and Shi 2015) including: retinotopic organization, receptive field size, variation of VC RF sizes with cortical depth and SF tuning curves. Hence, BOLD-fMRI signals faithfully represent these specific features while offering a very high resolution, longitudinal investigation, and a comprehensive whole-pathway vantage point. To the best of our knowledge, our work is the first fMRI-based retinotopic mapping and SF tuning curves in the rat visual pathway, and we note that the high-resolution (125x125 $\mu m^2$) population RFs that could be mapped using this approach can probably be extended in the future using denoising techniques (Ades-Aron et al. 2021; Veraart et al. 2016) and/or adaptation of the system to cryogenic coils (Labbé et al. 2021; Ratering et al. 2008; Baltes et al. 2009).

Once all the important features of the visual pathway were reproduced using BOLD-fMRI contrast, we could harness this approach towards investigating plasticity and stability in the visual pathway - in particular, how VDM affects the function and organization of the brain and how the visual experience promotes reorganization. Our main findings are: (1) The adult rat brain is highly plastic and that visual deprivation delays the maturation of RFs, in particular visually deprived animals lack retinotopic organization and SF specialization of the visual pathway; and (2) Light

exposure during adulthood (post-critical period) clearly promoted an extensive topographic remapping and functional specialization of the visual system in DR rats. At the level of BOLD signals, we show that the VDM affects the activation magnitude and timing of the responses. Then, using biologically inspired computational models of the RFs applied to the BOLD-signals in response to the complex stimuli, more perceptual features of the pathway could be unraveled, including that exposure to light upon visual deprivation opens a window of plasticity during adulthood that promotes specialization of the pathway towards normal vision. This unique view of the whole pathway, is promising for future characterisations of plasticity in health and disease. In a clinical context this technique holds the potential to assess the optimal timing for visual restoration and rehabilitation therapies, such as retinal stem cell transplantation, and to be pivotal for the translation of preclinical findings to humans. Below we discuss our findings and their implications in detail.

## 3.1 Visually deprived rats exhibit different BOLD response patterns compared to healthy controls which tend to normalize following visual experience

### 3.1.1 VC and LGN: Visual deprivation model modifies BOLD-fMRI response's amplitude and timing

The VC and LGN of visually deprived rats from birth, at the first moment of light exposure (t=0) showed an early onset time and the DR's VC and stronger BOLD responses compared to normal reared rats. This may reflect: 1) changes in excitation/inhibition balance of the visual cortex, most likely a reduction of inhibitory signals (Fierro et al. 2005; Castaldi, Lunghi, and Morrone 2020; Lunghi, Burr, and Morrone 2011) and 2) an adaptation mechanism through increase of contrast-gain, which results in enhanced excitability of the visual cortex following visual deprivation

(Boroojerdi et al. 2000). This cortical increase in gain-control reflects the adaptation mechanisms attempting to optimize weak or absent information during the visual deprivation period. Furthermore, similar mechanisms have also been described in humans, in which short-term monocular patching boosts the patched eye's response in the visual cortex (Jiawei Zhou et al. 2015; J. Zhou, Clavagnier, and Hess 2013; Lunghi, Burr, and Morrone 2011; Boroojerdi et al. 2000) and short-term binocular visual deprivation increases the excitability of the visual cortex (Boroojerdi et al. 2000). However, our results are in contrast with a previous study using ultra-fast fMRI which showed delayed, broad and low amplitude BOLD responses measured in the DR mice when compared to HCs (Gil, Fernandes, and Shemesh 2021). Two major differences between this study and (Gil, Fernandes, and Shemesh 2021) are that they used simple low frequency flickering visual stimuli and the visual stimulation was monocular. The size and content of the stimulus, the contrast, the spatial frequency and the movement direction very likely influenced the dynamics of the measured BOLD-fMRI responses and are likely to originate the differences between the studies.

Furthermore, we examined the BOLD-fMRI responses at multiple time points following light exposure. After one week of light exposure the BOLD responses to the retinotopy and SF tuning stimuli in the DR group returned to the level of HCs, reflecting that the window of plasticity (or critical period) in DR rats has been extended. This extension could be mediated by modification of excitatory–inhibitory balances (Vogels et al. 2011; Takao K. Hensch and Fagiolini 2005) and/or removal of brakes on plasticity (Bavelier et al. 2010; Erchova et al. 2017).

### 3.1.2 SC: Visual deprivation elicits negative BOLD responses to retinotopic stimuli in superior colliculus

For all the time points, the SC in dark reared animals showed a different behaviour to that described above for VC and LGN. In particular, SC exhibited a negative BOLD response contrasting with the positive BOLD response measured in HC. Although interpretation of negative BOLD responses is ambiguous, mounting evidence suggests that negative BOLD responses correlate with local decreases in neural activity (Shmuel et al. 2006; Boorman et al. 2010). One possible explanation for the negative BOLD responses observed in the DR group is enhanced intracortical or tecto-tectal inhibition (Goodale 1973). Previous studies have shown that visual deprivation potentiates inhibitory feedback and that it reflects a degradation of the visual function (Sten et al. 2017; Maffei et al. 2006; Kannan et al. 2016; Miska et al. 2018). The fact that the enhanced intracortical inhibition mostly affects SC is likely linked with the fact that SC receives mostly direct retinal inputs and it has a classical RF with excitatory center and an inhibitory surround (Prévost, Lepore, and Guillemot 2007; X. Li, Sun, and Shi 2015). The inhibitory inputs lead to an enhancement of surround suppression. Some studies suggest that early but not late light exposure protects against the effects of adult visual deprivation on the SC (Pallas 2009).

### 3.1.3 Differential vascular responses are not the underlying sources of the differences in BOLD responses observed between DR and HC

Negative BOLD can also be driven by reduced cerebral blood volume, a mechanism known as "vascular stealing" (Harel et al. 2002). To discard that differences in vasculature between DR and HC are the dominant driving force for the differential BOLD-fMRI responses observed between the two groups, a hypercapnia challenge was performed. Hypercapnia is a strong vasodilator, causing increases in cerebral blood flow and cerebral blood volume and it is used to calibrate

BOLD fMRI (Chen and Pike 2010). We found that the rise times and signal amplitude were nearly identical between DR and HC for the different ROIs, Figure S3. This suggests that vascular responses are similar between the groups and further pointing towards the differences being driven mainly by neural activity.

## 3.2 Refinement of receptive fields following light exposure during adulthood in dark reared animals across the entire visual pathway

### 3.2.1 Mapping non-invasive high resolution population receptive field properties

The VC does not receive a direct input from the retina. The activity of rodent VC neurons is driven by the geniculate pathway which projects feedforward visual information to layer IV of VC and by SC (which receives direct input from the retina) that projects broadly to all cortical layers of VC (Priebe and McGee 2014). Therefore, the ability of cortical neurons to integrate visual information varies across visual areas, while SC has limited spatial integration, VC integrated information over a large area (Prévost, Lepore, and Guillemot 2007; X. Li, Sun, and Shi 2015). This notion is in line with our results, as we found that the superficial layer of SC has the smallest receptive fields (~12º), while VC and LGN have larger sizes, 15º and 18º respectively. This also agrees with previous electrophysiology studies and corroborates the view that SC has limited spatial integration. Regarding the RF profiles across cortical layers, in the VC the population RF sizes are the largest at most superficial and deepest layers and smallest at layers IV and V. This is in agreement with electrophysiological studies in cats and human high-field fMRI (Fracasso, Petridou, and Dumoulin 2016; Gilbert 1977). The variation of the RF across cortical layers is linked to the flow of signals across the cortical architecture (Fracasso, Petridou, and Dumoulin 2016).

### 3.2.2 Visual experience following dark rearing promotes a pathway wide receptive field remapping and specialization (shrinkage)

We mapped the specialization of the visual pathway in DR rats during light exposure. Immediately after light exposure, VC, LGN and SC lacked retinotopic organization, the phase maps were totally disorganized when compared to the HC ones. With the continuous light exposure the visual pathway progressively became retinotopically organized, VC and LGN reached at t=27d the same level of retinotopic organization as HC. Although SC progressively reorganized, at t=27d it did not have reached the same level of reorganization as HC. Across the entice visual pathway the progressige organization of the visual pathways was accompanied by a shrinkage in pRF sizes. The pRF shrinkage took place during the first week of light exposure, and it stabilized and t=17d and t=27d. The fact that DR's RF size stabilizes before the retinotopic structure suggests that the shrinkage of RF is the driving force for the reorganization of the retinotopic structure. Our results agree with previous electrophysiology and calcium studies which locally showed that, in DR adult animals, the RF sizes of visual cortical neurons remain large (Fagiolini et al. 1994; Regal et al. 1976; Teller et al. 1978). Furthermore the refinement of RFs and SF curves corroborates the notion that dark rearing slows down the maturation of brakes on plasticity and that visual experience acts by modulating the level and the patterning of neural activity within the visual pathways.

## 3.3 Visual experience refines spatial frequency tuning curves

To investigate how visual deprivation affects the functioning of the visual pathways we estimated for the first-time the SF tuning curve across the rat visual pathway using fMRI. In general the neural populations in VC, LGN and SC respond to SFs between 0.02 and 0.16 cpd, with an average optimal SF estimated for VC, LGN and SC of 0.12; 0.07 and 0.05, respectively and based on HC

462 data. Furthermore we tracked the dynamic in the SF tuning curves in HC and DR from the first
463 moment to 27 days after light exposure.We found when first exposed to light the DR rats show
464 broader tuning curves than HC. One week after light exposure the tuning curves became sharper
465 (narrower and with an aligned peak with HC tuning curves), which suggests an increase in
466 selectivity. This was evident in SC, LGN and VC. Note that the tuning curves obtained for HC are
467 stable over time. These findings are in line with calcium and electrophysiology studies in mice
468 which have shown: a) that SF shifts are accompanied by a decreased tuning bandwidth (Vreysen
469 et al. 2012); and b) the DR delays the maturation on the cutoff SF (highest sinusoidal grating
470 frequency detectable by the visual system) (Zhang et al. 2015). However Zhang and colleagues
471 showed that DR mice showed lower SF cutoffs compared to HCs whereas our results indicate that
472 at t=0 DRs have higher SF cutoffs than HCs. Furthermore the refinement of SF tuning curves
473 tightly links with the results regarding the refinement of the RF over time, once large RF have a
474 preference for low spatial frequencies and vice versa. Similar patterns were also observed in
475 electrophysiology studies where the topographic refinement was accompanied by a decrease in
476 spot size preference and an increase in surround suppression (Tschetter et al. 2018).

477 In summary, our findings suggest that the VDM prevents the maturation of the RFs, as they
478 remain large without spatial/Sf selectivity and simultaneously VDM extends the critical period.
479 Visual experience during adulthood promotes the specialization of the RFs to maturation level
480 similar to the one of healthy controls.

## 481 3.4 Limitations and Future Research

482 During scanning the animals were sedated. Although medetomidine has been shown to be suitable
483 for the longitudinal studies (Weber et al. 2006), it can introduce bias compared to the awake state

due. One way to eliminate the anesthesia effect is to perform the experiments in awake animals, however this requires prolonged training to scanner noises and to the visual stimulus (to maintain a stable fixation throughout the experiment) which would be very difficult in DR animals. Another limitation of the study is that although the DR animals were kept in a dark room from birth, husbandry was performed under red light. A recent study has shown that although rats do not possess red cones, their visual capacity under red light is still preserved (Nikbakht and Diamond 2021). Hence, the animals are not "completely" deprived of light, but their visual pathways can still be expected to be highly immature.

Despite the usefulness of BOLD-fMRI, its neuronal underpinnings are still controversial (Logothetis 2003). To better dissect the origins of the observed BOLD responses simultaneous electrical recordings, calcium recordings and/ or optical imaging could be fruitfully applied (Lake et al. 2020; Wang et al. 2018; Liang et al. 2017).

# 4. Conclusion

This study illustrates how high-resolution fMRI, in combination with complex visual stimulation, can bridge the spatiotemporal scales necessary for repeatedly interrogating structural and functional changes underlying plasticity and longitudinally investigate how the stability/plasticity balance is sculpted by visual experience. Besides its relevance to understand the foundation of vision and plasticity, the findings of this study will form the basis for future assessment of the effect of retinal degeneration on visual function and the efficacy of any therapeutic intervention in animal models of retinal degeneration.

# 5. Materials and Methods

All the experiments strictly adhered to the ethical and experimental procedures in agreement with Directive 2010/63 of the European Parliament and of the Council, and were preapproved by the competent institutional (Champalimaud Animal Welfare Body) and national (Direcção Geral de Alimentação e Veterinária, DGAV) authorities.

## 5.1 Dark rearing

In this study, N=20 Adult Long Evan rats (N=18 Females, 12-20 weeks old, mean weight 322 g; range: 233-445 g) were used. The animals were randomly assigned into two groups: healthy controls (HC, N=10) and dark reared (DR, N=10). The DR animals were born and kept in the dark until 10-12 weeks of age with *ad libitum* access to food and water. Specifically, the animals were housed in a sound protected dark room. The husbandry and animal preparation for the MRI scanners were performed using red light (for which the animals are blind). They were first exposed to light during the first MRI scan (t=0). Thereafter, the DR animals were housed in a normal environment with a 12h light/12h dark cycle. Follow-up scans took place 7, 17 and 27 days after t=0. The normal reared HC rats were scanned following the same protocol but were born and kept in the normal environment (12 h/12 h light/dark cycle) from birth. The experiment timeline is shown in Figure 1E.

## 5.2 Animal preparation

All in-vivo experiments were performed under sedation. The animals were induced into deep anesthesia in a custom box with a flow of 5% isoflurane (Vetflurane, Virbac, France) mixed

with oxygen-enriched medical air for ~2 min. Once sedated, the animals were moved to a custom MRI animal bed (Bruker Biospin, Karlsruhe, Germany) and maintained under ~2.5–3.5% isoflurane while being prepared for imaging. The animals were placed 2.5 cm from a screen, where the stimuli were projected, and eye drops (Bepanthen, Bayer, Leverkusen, Germany) were applied to prevent the eyes from drying during anesthesia. Approximately 5 minutes after the isoflurane induction, a bolus (0.05 mg/kg) of medetomidine (Dormilan, Vetpharma Animal Health, Spain) consisting of a 1 mg/ml solution diluted 1:10 in saline was administered subcutaneously. Ten to eighteen minutes after the bolus, a constant infusion of 0.1 mg/kg/h of medetomidine, delivered via a syringe pump (GenieTouch, Kent Scientific, Torrington, Connecticut, USA), was started. During the period between the bolus and the beginning of the constant infusion, isoflurane was progressively reduced until reaching 0%.

Temperature and respiration rate were continuously monitored via a rectal optic fiber temperature probe and a respiration sensor (Model 1025, SAM-PC monitor, SA Instruments Inc., USA), respectively, and remained constant throughout the experiment. Each MRI session lasted between 2h30 and 3h. At the end of each MRI session, to revert the sedation, 2.0 mg/kg of atipamezole (5 mg/ml solution diluted 1:10 in saline) (Antisedan, Vetpharma Animal Health, Spain) was injected subcutaneously at the same volume of the initial bolus.

## 5.3 MRI acquisition

All the MRI scans were performed using a 9.4T Bruker BioSpin MRI scanner (Bruker, Karlsruhe, Germany) operating at a $^{1}$H frequency of 400.13 MHz and equipped with an AVANCE III HD console and a gradient system capable of producing up to 660 mT/m isotropically. An 86

mm volume quadrature resonator was used for transmittance and a 20 mm loop surface coil was used for reception. The software running on this scanner was ParaVision® 6.0.1.

After placing the animal in the scanner bed, localizer scans were performed to ensure that the animal was correctly positioned and routine adjustments were performed. B0 maps were acquired. A high-definition anatomical $T_2$-weighted Rapid Acquisition with Refocused Echoes (RARE) sequence (TE/TR = 13.3/2000 ms, RARE factor = 5, FOV = 20 × 16 $mm^2$, in-plane resolution = 80 × 80 $\mu m^2$, slice thickness = 500 μm, $t_{acq}$ = 1 min 18 s) was acquired for accurate referencing. Functional scans were acquired using a gradient-echo echo-planar imaging (GE-EPI) sequence (TE/TR = 16.7/1500 ms, FOV = 20.5 × 15 $mm^2$, resolution = 125 × 125 $\mu m^2$, slice thickness = 650 μm, 12 slices covering the visual pathway, flip angle = 15º). Importantly, the functional MRI scans were started ~30 min after the isoflurane was removed from the breathing air to avoid the potentially confounding effects of isoflurane (Tsurugizawa, Takahashi, and Kato 2016; Wu et al. 2016; Masamoto et al. 2007).

We performed two types of visual stimulus: retinotopy mapping and spatial frequency tuning. The animals underwent a total of 6 runs of the retinotopic stimulus, each run taking 7 min and 39 s to acquire (306 repetitions), and 2 runs of spatial frequency tuning experiment, each lasting 12 min and 15 s (490 repetitions).

## 5.4 Visual stimulus delivery setup and paradigm

### 5.4.1 Setup

The complex visual stimuli necessary for retinotopic mapping, insofar never achieved in rodent fMRI, were generated outside the scanner and back-projected with an Epson EH-TW7000 projector onto a semitransparent screen positioned 2.5 cm from the animals eyes (Figure 1A and

B). The projector was located in the scanner room outside the fringe field. An acrylic mirror of 30×30 $cm^2$ was positioned ~2 meters from the projector and ~2.6 meters from the animal. The mirror was angled at 45º so that the light coming from the projector was reflected with a 90º angle towards the scanner bore. The light was focused in a semi-circular screen with 4 cm radius, resulting in a field of view of ~116º of visual angle. A scheme of the setup is shown on Figure 1A. The animals viewed the stimulus binocularly. Using this setup, two sets of stimuli were presented: a retinotopy stimulus which allows us to derive the population receptive field parameters, and a spatial frequency tuning stimulus. Visual stimuli were created using MATLAB (Mathworks, Natick, MA, USA) and the Psychtoolbox (Brainard 1997; Pelli 1997). An Arduino MEGA260 receiving triggers from the MRI scanner was used to control stimuli timings.

### 5.4.2 Retinotopy

The visual stimuli consisted of a luminance contrast-inverting checkerboard drifting bar (Dumoulin and Wandell 2008). The bar aperture was composed by alternating rows of high-contrast luminance checks moved in 8 different directions (4 bar orientations: horizontal, vertical and the two diagonal orientations, with two opposite drift directions for each orientation, Figure 1C). The bar moved across the screen in 16 equally spaced steps, each lasting 1 TR. The bar contrast, width, and spatial frequency were 50%, ~14.5º, and ~0.2 cycles per degree of visual angle (cpd), respectively. The retinotopic stimulus consisted of four stimulation blocks. At each stimulation block, the bar moved across the entire screen during 24 s (swiping the visual field in the horizontal or vertical directions) and across half of the screen for 12 s (swiping half of the visual field diagonally), followed by a blank full screen stimulus at mean luminance for 45 s, Figure 1C. A single retinotopic mapping run consisted of 246 functional images (60 pre-scan images were deliberately planned to be discarded due to coil heating).

### 5.4.3 Spatial frequency tuning

The stimulus consisted of a block design on/off task, with a baseline of 45 s which consisted of a black screen, and an activation task of 15 s (Figure 1D), in a total of 10 stimulation blocks. The activation stimulus consisted of vertical sinusoidal gratings of multiple spatial frequencies: 0.003, 0.02, 0.04, 0.08, 0.1, 0.16, 0.20, 0.25, 0.36, 0.5 cpd moving left to right at 5 Hz. The SF stimulation blocks were randomized. The grating contrast was 100%. A single retinotopic mapping run consisted of 430 functional images (60 pre-scan images were deliberately planned to be discarded due to coil heating).

## 5.5 Hypercapnia

A hypercapnia experiment was performed to determine the influence of the vascular component in putative changes in activation, retinotopic maps and SF tuning curves, and to disentangle between the neural and vascular components of the BOLD responses in multiple regions of the visual pathway. To achieve this, N=10 additional animals (N=6 Females, 12-28 weeks old, median weight 340 g; range 285-470 g) underwent the hypercapnia condition (DR, N=5, HC, N=5). The animals performed the hypercapnia condition at t=0. The hypercapnia paradigm consisted of 90 s ventilation with medical air followed by a manual switch to a hypercapnia state with 6.5% $CO_2$ for 90 s. In the end of the hypercapnia period, the $CO_2$ was switched off, the animals resumed breathing medical air and data kept being acquired for 1.5 additional minutes. In between hypercapnia “runs”, the animals rested for 2 minutes.

# 5.6 Data Analysis

## 5.6.1 Preprocessing

The images were first converted to Nifti. Then, outlier correction was performed (time points whose signal intensity was 3 times higher or lower than the standard deviation of the entire time course were replaced by the mean of the 3 antecedent and 3 subsequent time points). Simultaneous motion and slice timing correction were performed using Nipy's SpaceTimeRealign function (Roche 2011). The brain extraction was done using AFNI function Automask applied to a bias field corrected (ANTs) mean functional image. The skull stripped images were inspected and upon visual inspection a further mask was manually drawn when needed using a home-written script. The skull stripped images then underwent co-registration and normalization to an atlas (Barrière et al. 2019). The co-registration alignment was performed by calculating the transform matrix that aligns the mean functional image of each run to the anatomical image, and normalization was performed by calculating the transform matrix that aligns each anatomical image with the atlas template. These two sets of matrices were then applied to all the runs per animal. Co-registration and normalization were performed in ANTs and, when necessary, manually adjusted using ITK SNAP. Following normalization, the voxels' signals were detrended using a polynomial function of factor 2 fitted to the resting periods and spatially smoothed (FWHM = 0.15 $mm^2$). All preprocessing steps were performed using a home-written Python pipeline using Nypipe. The code is available for free download at https://github.com/Joana-Carvalho.

## 5.6.2 ROI analysis

Five regions of interest (ROIs) were defined according to the SIGMA atlas (Barrière et al. 2019) and manually adjusted per animal. These ROIs comprehended different visual pathway structures such as the binocular visual cortex (VC), the lateral geniculate nucleus (LGN) and the superior layer of the superior colliculus (SC). The detrended time series of the voxels comprising each ROI were converted into percentage signal change (PSC) and averaged across epochs, runs and animals providing the averaged response within each region per acquisition time point. The 25%, 50% and 75% percentiles per ROI were also calculated (Figures 4, S1 and S2).

### 5.6.3 Retinotopic mapping analysis

Retinotopic mapping analysis was performed using both conventional population receptive field (pRF) mapping (Dumoulin and Wandell 2008) and micro-probing (Carvalho et al., n.d.). In brief, these methods model the population of neurons measured within a voxel as a two-dimensional Gaussian, where the center corresponds to the pRF's position and the width to its size.

#### 5.6.3.1 Conventional pRF mapping

In the conventional method, a 2D-Gaussian model $n(x, y)$ was fitted with parameters: center ($x_0$, $y_0$) and size ($\sigma$ - width of the Gaussian), for each voxel.

$$n(x,y) = e^{\frac{(x-x_0)^2+(y-y_0)^2}{-2\sigma^2}} \qquad \text{Eq. 1}$$

The predicted response of a voxel $p(t)$ to the stimulus was then calculated as the overlap between the stimulus mask (binary image of the stimulus aperture over time: $s(x, y, t)$) at each time point and the neural model $n(x, y)$.

$$p(t) = \sum_{x,y} \quad s(x,y,t) * n(x,y) \qquad \text{Eq. 2}$$

Subsequently, the delay in hemodynamic response was accounted for by convolving the predicted time courses with a haemodynamic response function (HRF) model consisting of a double-gamma function with a peak at 1.4 s. Finally, the pRF model parameters were adjusted for each cortical location to minimize the difference between the prediction and the measured BOLD data. The best fitting parameters are the output of the analysis.

The pRF properties estimation was performed using a home-written script. The data was thresholded by retaining the pRF models that explained at least 5% of the variance.

#### 5.6.3.2 Micro-probing

Micro-probing applies large numbers of "micro-probes", 2D-Gaussians with a narrow standard deviation, to sample the entire stimulus space and create high-resolution probe maps. The number of micro-probes included, 10000, was calculated based on the trade off between achieving a good coverage of the visual field and the time to compute a probe map. Like the conventional pRF approach, these micro-probes sample the aggregate response of neuronal subpopulations, but they do so at a much higher spatial resolution. Consequently, for each voxel, the micro-probing generates a RF profile representing the density and variance explained (VE) for all the probes.

### 5.6.4 General Linear Model (GLM) analysis

For the statistical t-maps, different GLMs were fitted, targeting (1) a per-subject analysis and (2) a group-level analysis. In all cases, each session from every animal was regressed with their respective realignment parameters and a double-gamma HRF (described in the previous section) convolved with the stimulation paradigm (contrast obtained using on and off blocks).

The t-values associated with the activation contrast were then mapped voxelwise. The maps were FDR corrected for multiple comparisons using a p-value of 0.001 and minimum cluster size of 20 voxels.

### 5.6.5 Spatial frequency analysis

The optimal SF per voxel was determined. First, we calculated the maximum BOLD modulation during the activation period of each individual activation block. The SF that elicited the strongest BOLD response was considered the optimal SF for that specific voxel.

The ROI specific tuning curves were obtained by calculating the optimal SF on the averaged ROI signal during the activation period of each individual activation block. Then, we plotted the BOLD magnitude (i.e., the maximum PSC) of the activation blocks as a function of the SF. Finally, we fitted a 1d Gaussian model to the SF turning curve:

$$SF_{tuning\ curve} = A \cdot e^{\frac{-(x-\mu)^2}{2\sigma^2}} \qquad \text{Eq. 3}$$

where the center ($\mu$) corresponds to the optimal SF and $\sigma$ to the broadness of the tuning curve.

# References


Ades-Aron, Benjamin, Gregory Lemberskiy, Jelle Veraart, John Golfinos, Els Fieremans, Dmitry S. Novikov, and Timothy Shepherd. 2021. "Improved Task-Based Functional MRI Language Mapping in Patients with Brain Tumors through Marchenko-Pastur Principal Component Analysis Denoising." *Radiology* 298 (2): 365–73.

Alves, Rita, Rafael Neto Henriques, Leevi Kerkelä, Cristina Chavarrías, Sune N. Jespersen, and Noam Shemesh. 2021. "Correlation Tensor MRI Deciphers Underlying Kurtosis Sources in Stroke." *NeuroImage*, December, 118833.

Baltes, Christof, Nicole Radzwill, Simone Bosshard, Daniel Marek, and Markus Rudin. 2009. "Micro MRI of the Mouse Brain Using a Novel 400 MHz Cryogenic Quadrature RF Probe." *NMR in Biomedicine* 22 (8): 834–42.

Barrière, D. A., R. Magalhães, A. Novais, P. Marques, E. Selingue, F. Geffroy, F. Marques, et al. 2019. "The SIGMA Rat Brain Templates and Atlases for Multimodal MRI Data Analysis and Visualization." *Nature Communications* 10 (1): 5699.

Baseler, Heidi A., André Gouws, Koen V. Haak, Christopher Racey, Michael D. Crossland, Adnan Tufail, Gary S. Rubin, Frans W. Cornelissen, and Antony B. Morland. 2011. "Large-Scale Remapping of Visual Cortex Is Absent in Adult Humans with Macular Degeneration." *Nature Neuroscience* 14 (5): 649–55.

Bavelier, Daphne, Dennis M. Levi, Roger W. Li, Yang Dan, and Takao K. Hensch. 2010. "Removing Brakes on Adult Brain Plasticity: From Molecular to Behavioral Interventions." *The Journal of Neuroscience: The Official Journal of the Society for Neuroscience* 30 (45): 14964–71.

Binns, K. E., and T. E. Salt. 1997. "Post Eye-Opening Maturation of Visual Receptive Field Diameters in the Superior Colliculus of Normal- and Dark-Reared Rats." *Brain Research. Developmental Brain Research* 99 (2): 263–66.

Boorman, L., A. J. Kennerley, D. Johnston, M. Jones, Y. Zheng, P. Redgrave, and J. Berwick. 2010. "Negative Blood Oxygen Level Dependence in the Rat:A Model for Investigating the Role of Suppression in Neurovascular Coupling." *Journal of Neuroscience*. https://doi.org/10.1523/jneurosci.6063-09.2010.

Boroojerdi, B., K. O. Bushara, B. Corwell, I. Immisch, F. Battaglia, W. Muellbacher, and L. G. Cohen. 2000. "Enhanced Excitability of the Human Visual Cortex Induced by Short-Term Light Deprivation." *Cerebral Cortex* 10 (5): 529–34.

Brainard, D. H. 1997. "The Psychophysics Toolbox." *Spatial Vision* 10 (4): 433–36.

Carvalho, Joana, Azzurra Invernizzi, Khazar Ahmadi, Michael B. Hoffmann, Remco J. Renken, and Frans W. Cornelissen. 2020. "Micro-Probing Enables Fine-Grained Mapping of Neuronal Populations Using fMRI." *NeuroImage* 209 (April): 116423.

———. n.d. "Micro-Probing Enables High-Resolution Mapping of Neuronal Subpopulations Using fMRI." https://doi.org/10.1101/709006.

Carvalho, Joana, Azzurra Invernizzi, Joana Martins, Nomdo M. Jansonius, Remco J. Renken, and Frans W. Cornelissen. 2021. "Visual Field Reconstruction Using fMRI-Based Techniques." *Translational Vision Science & Technology* 10 (1): 25.

Castaldi, Elisa, Claudia Lunghi, and Maria Concetta Morrone. 2020. "Neuroplasticity in Adult Human Visual Cortex." *Neuroscience & Biobehavioral Reviews*. https://doi.org/10.1016/j.neubiorev.2020.02.028.

Chen, J. Jean, and G. Bruce Pike. 2010. "Global Cerebral Oxidative Metabolism during Hypercapnia and Hypocapnia in Humans: Implications for BOLD fMRI." *Journal of Cerebral Blood Flow and Metabolism: Official Journal of the International Society of Cerebral Blood Flow and Metabolism* 30 (6): 1094–99.

Daw, N. W., K. Fox, H. Sato, and D. Czepita. 1992. "Critical Period for Monocular Deprivation in the Cat Visual Cortex." *Journal of Neurophysiology* 67 (1): 197–202.

Dijkhuizen, R. M., M. van Lookeren Campagne, T. Niendorf, W. Dreher, A. van der Toorn, M. Hoehn-Berlage, H. B. Verheul, et al. 1996. "Status of the Neonatal Rat Brain after NMDA-Induced Excitotoxic Injury as Measured by MRI, MRS and Metabolic Imaging." *NMR in Biomedicine* 9 (2): 84–92.

Di Marco, Stefano, Vincent A. Nguyen, Silvia Bisti, and Dario A. Protti. 2009. "Permanent Functional Reorganization of Retinal Circuits Induced by Early Long-Term Visual Deprivation." *The Journal of Neuroscience: The Official Journal of the Society for Neuroscience* 29 (43): 13691–701.

Dodwell, P. C. 1961. "Visual Orientation Preferences in the Rat." *Quarterly Journal of Experimental Psychology*. https://doi.org/10.1080/17470216108416467.

Dräger, U. C. 1975. "Receptive Fields of Single Cells and Topography in Mouse Visual Cortex." *The Journal of Comparative Neurology* 160 (3): 269–90.

Dumoulin, Serge O., and Brian A. Wandell. 2008. "Population Receptive Field Estimates in Human Visual Cortex."

*NeuroImage* 39 (2): 647–60.
Dunn, Felice A., Luca Della Santina, Edward D. Parker, and Rachel O. L. Wong. 2013. "Sensory Experience Shapes the Development of the Visual System's First Synapse." *Neuron* 80 (5): 1159–66.
Eimer, Martin. 2004. "Multisensory Integration: How Visual Experience Shapes Spatial Perception." *Current Biology: CB* 14 (3): R115–17.
Erchova, Irina, Asta Vasalauskaite, Valentina Longo, and Frank Sengpiel. 2017. "Enhancement of Visual Cortex Plasticity by Dark Exposure." *Philosophical Transactions of the Royal Society of London. Series B, Biological Sciences* 372 (1715). https://doi.org/10.1098/rstb.2016.0159.
Espinoza, S. G., and H. C. Thomas. 1983. "Retinotopic Organization of Striate and Extrastriate Visual Cortex in the Hooded Rat." *Brain Research* 272 (1): 137–44.
Fagiolini, M., T. Pizzorusso, N. Berardi, L. Domenici, and L. Maffei. 1994. "Functional Postnatal Development of the Rat Primary Visual Cortex and the Role of Visual Experience: Dark Rearing and Monocular Deprivation." *Vision Research* 34 (6): 709–20.
Fierro, Brigida, Filippo Brighina, Gaetano Vitello, Aurelio Piazza, Simona Scalia, Giuseppe Giglia, Ornella Daniele, and Alvaro Pascual-Leone. 2005. "Modulatory Effects of Low- and High-Frequency Repetitive Transcranial Magnetic Stimulation on Visual Cortex of Healthy Subjects Undergoing Light Deprivation." *The Journal of Physiology* 565 (Pt 2): 659–65.
Fracasso, Alessio, Natalia Petridou, and Serge O. Dumoulin. 2016. "Systematic Variation of Population Receptive Field Properties across Cortical Depth in Human Visual Cortex." *NeuroImage* 139 (October): 427–38.
Gianfranceschi, Laura, Rosita Siciliano, Jennifer Walls, Bernardo Morales, Alfredo Kirkwood, Z. Josh Huang, Susumu Tonegawa, and Lamberto Maffei. 2003. "Visual Cortex Is Rescued from the Effects of Dark Rearing by Overexpression of BDNF." *Proceedings of the National Academy of Sciences of the United States of America* 100 (21): 12486–91.
Gilbert, C. D. 1977. "Laminar Differences in Receptive Field Properties of Cells in Cat Primary Visual Cortex." *The Journal of Physiology* 268 (2): 391–421.
Gil, Rita, Francisca F. Fernandes, and Noam Shemesh. 2021. "Neuroplasticity-Driven Timing Modulations Revealed by Ultrafast Functional Magnetic Resonance Imaging." *NeuroImage*. https://doi.org/10.1016/j.neuroimage.2020.117446.
Girman, S. V., Y. Sauvé, and R. D. Lund. 1999. "Receptive Field Properties of Single Neurons in Rat Primary Visual Cortex." *Journal of Neurophysiology* 82 (1): 301–11.
Goodale, M. A. 1973. "Cortico-Tectal and Intertectal Modulation of Visual Responses in the Rat's Superior Colliculus." *Experimental Brain Research. Experimentelle Hirnforschung. Experimentation Cerebrale* 17 (1): 75–86.
Harel, Noam, Sang-Pil Lee, Tsukasa Nagaoka, Dae-Shik Kim, and Seong-Gi Kim. 2002. "Origin of Negative Blood Oxygenation Level-Dependent fMRI Signals." *Journal of Cerebral Blood Flow and Metabolism: Official Journal of the International Society of Cerebral Blood Flow and Metabolism* 22 (8): 908–17.
Hensch, Takao K., and Michela Fagiolini. 2005. "Excitatory–inhibitory Balance and Critical Period Plasticity in Developing Visual Cortex." In *Progress in Brain Research*, 147:115–24. Elsevier.
Hensch, T. K., M. Fagiolini, N. Mataga, M. P. Stryker, S. Baekkeskov, and S. F. Kash. 1998. "Local GABA Circuit Control of Experience-Dependent Plasticity in Developing Visual Cortex." *Science* 282 (5393): 1504–8.
Hoehn, Mathias, Klaas Nicolay, Claudia Franke, and Boudewijn van der Sanden. 2001. "Application of Magnetic Resonance to Animal Models of Cerebral Ischemia." *Journal of Magnetic Resonance Imaging*. https://doi.org/10.1002/jmri.1213.
Hooks, Bryan M., and Chinfei Chen. 2007. "Critical Periods in the Visual System: Changing Views for a Model of Experience-Dependent Plasticity." *Neuron* 56 (2): 312–26.
Hoy, Jennifer L., and Cristopher M. Niell. 2015. "Layer-Specific Refinement of Visual Cortex Function after Eye Opening in the Awake Mouse." *The Journal of Neuroscience: The Official Journal of the Society for Neuroscience* 35 (8): 3370–83.
Hubel, D. H., and T. N. Wiesel. 1962. "Receptive Fields, Binocular Interaction and Functional Architecture in the Cat's Visual Cortex." *The Journal of Physiology*. https://doi.org/10.1113/jphysiol.1962.sp006837.
———. 1970. "The Period of Susceptibility to the Physiological Effects of Unilateral Eye Closure in Kittens." *The Journal of Physiology* 206 (2): 419–36.
Hübener, Mark, and Tobias Bonhoeffer. 2014. "Neuronal Plasticity: Beyond the Critical Period." *Cell* 159 (4): 727–37.
Huberman, Andrew D., Marla B. Feller, and Barbara Chapman. 2008. "Mechanisms Underlying Development of Visual Maps and Receptive Fields." *Annual Review of Neuroscience* 31 (1): 479–509.

802 Iwai, Youichi, Michela Fagiolini, Kunihiko Obata, and Takao K. Hensch. 2003. "Rapid Critical Period Induction by
803 Tonic Inhibition in Visual Cortex." *The Journal of Neuroscience: The Official Journal of the Society for*
804 *Neuroscience* 23 (17): 6695–6702.
805 Jenks, Kyle R., and Jason D. Shepherd. 2020. "Experience-Dependent Development and Maintenance of Binocular
806 Neurons in the Mouse Visual Cortex." *Cell Reports* 30 (6): 1982–94.e4.
807 Kaas, J. H., L. A. Krubitzer, Y. M. Chino, A. L. Langston, E. H. Polley, and N. Blair. 1990. "Reorganization of
808 Retinotopic Cortical Maps in Adult Mammals after Lesions of the Retina." *Science* 248 (4952): 229–31.
809 Kalia, Amy, Luis Andres Lesmes, Michael Dorr, Tapan Gandhi, Garga Chatterjee, Suma Ganesh, Peter J. Bex, and
810 Pawan Sinha. 2014. "Development of Pattern Vision Following Early and Extended Blindness." *Proceedings of*
811 *the National Academy of Sciences of the United States of America* 111 (5): 2035–39.
812 Kannan, Madhuvanthi, Garrett G. Gross, Don B. Arnold, and Michael J. Higley. 2016. "Visual Deprivation During
813 the Critical Period Enhances Layer 2/3 GABAergic Inhibition in Mouse V1." *The Journal of Neuroscience:*
814 *The Official Journal of the Society for Neuroscience* 36 (22): 5914–19.
815 Keck, Tara, Thomas D. Mrsic-Flogel, Miguel Vaz Afonso, Ulf T. Eysel, Tobias Bonhoeffer, and Mark Hübener.
816 2008. "Massive Restructuring of Neuronal Circuits during Functional Reorganization of Adult Visual Cortex."
817 *Nature Neuroscience* 11 (10): 1162–67.
818 Keck, Tara, Volker Scheuss, R. Irene Jacobsen, Corette J. Wierenga, Ulf T. Eysel, Tobias Bonhoeffer, and Mark
819 Hübener. 2011. "Loss of Sensory Input Causes Rapid Structural Changes of Inhibitory Neurons in Adult Mouse
820 Visual Cortex." *Neuron* 71 (5): 869–82.
821 Koehler, Christopher L., Nikolay P. Akimov, and René C. Rentería. 2011. "Receptive Field Center Size Decreases
822 and Firing Properties Mature in ON and OFF Retinal Ganglion Cells after Eye Opening in the Mouse." *Journal*
823 *of Neurophysiology* 106 (2): 895–904.
824 Labbé, Aimé, Gilles Authelet, Bertrand Baudouy, Cornelis J. van der Beek, Javier Briatico, Luc Darrasse, and Marie
825 Poirier-Quinot. 2021. "Recent Advances and Challenges in the Development of Radiofrequency HTS Coil for
826 MRI." *Frontiers of Physics* 9 (July). https://doi.org/10.3389/fphy.2021.705438.
827 Lake, Evelyn M. R., Xinxin Ge, Xilin Shen, Peter Herman, Fahmeed Hyder, Jessica A. Cardin, Michael J. Higley, et
828 al. 2020. "Simultaneous Cortex-Wide Fluorescence Ca2+ Imaging and Whole-Brain fMRI." *Nature Methods*
829 17 (12): 1262–71.
830 Liang, Zhifeng, Yuncong Ma, Glenn D. R. Watson, and Nanyin Zhang. 2017. "Simultaneous GCaMP6-Based Fiber
831 Photometry and fMRI in Rats." *Journal of Neuroscience Methods* 289 (September): 31–38.
832 Li, Man-Zhong, Yi Zhang, Hai-Yan Zou, Jun-Yao Ouyang, Yu Zhan, Le Yang, Brian Chi-Yan Cheng, et al. 2018.
833 "Investigation of Ginkgo Biloba Extract (EGb 761) Promotes Neurovascular Restoration and Axonal
834 Remodeling after Embolic Stroke in Rat Using Magnetic Resonance Imaging and Histopathological Analysis."
835 *Biomedicine & Pharmacotherapy = Biomedecine & Pharmacotherapie* 103 (July): 989–1001.
836 Li, Xiaoyuan, Chaokui Sun, and Li Shi. 2015. "Comparison of Visual Receptive Field Properties of the Superior
837 Colliculus and Primary Visual Cortex in Rats." *Brain Research Bulletin* 117 (August): 69–80.
838 Logothetis, Nikos K. 2003. "The Underpinnings of the BOLD Functional Magnetic Resonance Imaging Signal."
839 *The Journal of Neuroscience: The Official Journal of the Society for Neuroscience* 23 (10): 3963–71.
840 Lunghi, Claudia, David C. Burr, and Concetta Morrone. 2011. "Brief Periods of Monocular Deprivation Disrupt
841 Ocular Balance in Human Adult Visual Cortex." *Current Biology: CB* 21 (14): R538–39.
842 Maffei, Arianna, Kiran Nataraj, Sacha B. Nelson, and Gina G. Turrigiano. 2006. "Potentiation of Cortical Inhibition
843 by Visual Deprivation." *Nature*. https://doi.org/10.1038/nature05079.
844 Masamoto, Kazuto, Tae Kim, Mitsuhiro Fukuda, Ping Wang, and Seong-Gi Kim. 2007. "Relationship between
845 Neural, Vascular, and BOLD Signals in Isoflurane-Anesthetized Rat Somatosensory Cortex." *Cerebral Cortex*
846 17 (4): 942–50.
847 Meliza, C. Daniel, and Yang Dan. 2006. "Receptive-Field Modification in Rat Visual Cortex Induced by Paired
848 Visual Stimulation and Single-Cell Spiking." *Neuron* 49 (2): 183–89.
849 Miska, Nathaniel J., Leonidas Ma Richter, Brian A. Cary, Julijana Gjorgjieva, and Gina G. Turrigiano. 2018.
850 "Sensory Experience Inversely Regulates Feedforward and Feedback Excitation-Inhibition Ratio in Rodent
851 Visual Cortex." *eLife* 7 (October). https://doi.org/10.7554/eLife.38846.
852 Moeller, Steen, Pramod Kumar Pisharady, Sudhir Ramanna, Christophe Lenglet, Xiaoping Wu, Logan Dowdle,
853 Essa Yacoub, Kamil Uğurbil, and Mehmet Akçakaya. n.d. "NOise Reduction with DIstribution Corrected
854 (NORDIC) PCA in dMRI with Complex-Valued Parameter-Free Locally Low-Rank Processing."
855 https://doi.org/10.1101/2020.08.25.267062.
856 Morales, Bernardo, Se-Young Choi, and Alfredo Kirkwood. 2002. "Dark Rearing Alters the Development of
857 GABAergic Transmission in Visual Cortex." *The Journal of Neuroscience: The Official Journal of the Society*

*for Neuroscience* 22 (18): 8084–90.
Mower, G. D. 1991. "The Effect of Dark Rearing on the Time Course of the Critical Period in Cat Visual Cortex." *Brain Research. Developmental Brain Research* 58 (2): 151–58.
Mower, G. D., and W. G. Christen. 1985. "Role of Visual Experience in Activating Critical Period in Cat Visual Cortex." *Journal of Neurophysiology* 53 (2): 572–89.
Nikbakht, Nader, and Mathew E. Diamond. 2021. "Conserved Visual Capacity of Rats under Red Light," July. https://doi.org/10.7554/eLife.66429.
Pallas, Sarah L. 2009. *Developmental Plasticity of Inhibitory Circuitry*. Springer.
Pelled, Galit, Kai-Hsiang Chuang, Stephen J. Dodd, and Alan P. Koretsky. 2007. "Functional MRI Detection of Bilateral Cortical Reorganization in the Rodent Brain Following Peripheral Nerve Deafferentation." *NeuroImage* 37 (1): 262–73.
Pelli, D. G. 1997. "The VideoToolbox Software for Visual Psychophysics: Transforming Numbers into Movies." *Spatial Vision* 10 (4): 437–42.
Prévost, François, Franco Lepore, and Jean-Paul Guillemot. 2007. "Spatio-Temporal Receptive Field Properties of Cells in the Rat Superior Colliculus." *Brain Research* 1142 (April): 80–91.
Priebe, Nicholas J., and Aaron W. McGee. 2014. "Mouse Vision as a Gateway for Understanding How Experience Shapes Neural Circuits." *Frontiers in Neural Circuits* 8 (October): 123.
Ratering, David, Christof Baltes, Jurek Nordmeyer-Massner, Daniel Marek, and Markus Rudin. 2008. "Performance of a 200-MHz Cryogenic RF Probe Designed for MRI and MRS of the Murine Brain." *Magnetic Resonance in Medicine*. https://doi.org/10.1002/mrm.21629.
Regal, D. M., R. Boothe, D. Y. Teller, and G. P. Sackett. 1976. "Visual Acuity and Visual Responsiveness in Dark-Reared Monkeys (Macaca Nemestrina)." *Vision Research* 16 (5): 523–30.
Roche, Alexis. 2011. "A Four-Dimensional Registration Algorithm with Application to Joint Correction of Motion and Slice Timing in fMRI." *IEEE Transactions on Medical Imaging* 30 (8): 1546–54.
Sherman, S. M., and P. D. Spear. 1982. "Organization of Visual Pathways in Normal and Visually Deprived Cats." *Physiological Reviews* 62 (2): 738–855.
Shmuel, Amir, Mark Augath, Axel Oeltermann, and Nikos K. Logothetis. 2006. "Negative Functional MRI Response Correlates with Decreases in Neuronal Activity in Monkey Visual Area V1." *Nature Neuroscience* 9 (4): 569–77.
Smith, Spencer L., and Joshua T. Trachtenberg. 2010. "The Refinement of Ipsilateral Eye Retinotopic Maps Is Increased by Removing the Dominant Contralateral Eye in Adult Mice." *PloS One* 5 (3): e9925.
Sriram, Balaji, Philip M. Meier, and Pamela Reinagel. 2016. "Temporal and Spatial Tuning of Dorsal Lateral Geniculate Nucleus Neurons in Unanesthetized Rats." *Journal of Neurophysiology* 115 (5): 2658–71.
Sten, S., K. Lundengård, S. T. Witt, G. Cedersund, F. Elinder, and M. Engström. 2017. "Neural Inhibition Can Explain Negative BOLD Responses: A Mechanistic Modelling and fMRI Study." *NeuroImage* 158 (September): 219–31.
Teller, D. Y., D. M. Regal, T. O. Videen, and E. Pulos. 1978. "Development of Visual Acuity in Infant Monkeys (Macaca Nemestrina) during the Early Postnatal Weeks." *Vision Research* 18 (5): 561–66.
Timney, B., D. E. Mitchell, and F. Giffin. 1978. "The Development of Vision in Cats after Extended Periods of Dark-Rearing." *Experimental Brain Research. Experimentelle Hirnforschung. Experimentation Cerebrale* 31 (4): 547–60.
Tschetter, Wayne W., Gubbi Govindaiah, Ian M. Etherington, William Guido, and Cristopher M. Niell. 2018. "Refinement of Spatial Receptive Fields in the Developing Mouse Lateral Geniculate Nucleus Is Coordinated with Excitatory and Inhibitory Remodeling." *The Journal of Neuroscience: The Official Journal of the Society for Neuroscience* 38 (19): 4531–42.
Tsurugizawa, Tomokazu, Yukari Takahashi, and Fusao Kato. 2016. "Distinct Effects of Isoflurane on Basal BOLD Signals in Tissue/vascular Microstructures in Rats." *Scientific Reports* 6 (December): 38977.
Veraart, Jelle, Dmitry S. Novikov, Daan Christiaens, Benjamin Ades-aron, Jan Sijbers, and Els Fieremans. 2016. "Denoising of Diffusion MRI Using Random Matrix Theory." *NeuroImage* 142 (November): 394–406.
Vogels, T. P., H. Sprekeler, F. Zenke, C. Clopath, and W. Gerstner. 2011. "Inhibitory Plasticity Balances Excitation and Inhibition in Sensory Pathways and Memory Networks." *Science* 334 (6062): 1569–73.
Vreysen, Samme, Bin Zhang, Yuzo M. Chino, Lutgarde Arckens, and Gert Van den Bergh. 2012. "Dynamics of Spatial Frequency Tuning in Mouse Visual Cortex." *Journal of Neurophysiology* 107 (11): 2937–49.
Wandell, Brian A., Serge O. Dumoulin, and Alyssa A. Brewer. 2007. "Visual Field Maps in Human Cortex." *Neuron* 56 (2): 366–83.
Wang, Maosen, Yi He, Terrence J. Sejnowski, and Xin Yu. 2018. "Brain-State Dependent Astrocytic Ca2+ Signals

914 Are Coupled to Both Positive and Negative BOLD-fMRI Signals." *Proceedings of the National Academy of*
915 *Sciences of the United States of America* 115 (7): E1647–56.
916 Weber, Ralph, Pedro Ramos-Cabrer, Dirk Wiedermann, Nadja van Camp, and Mathias Hoehn. 2006. "A Fully
917 Noninvasive and Robust Experimental Protocol for Longitudinal fMRI Studies in the Rat." *NeuroImage* 29 (4):
918 1303–10.
919 Womelsdorf, Thilo, Katharina Anton-Erxleben, Florian Pieper, and Stefan Treue. 2006. "Dynamic Shifts of Visual
920 Receptive Fields in Cortical Area MT by Spatial Attention." *Nature Neuroscience* 9 (9): 1156–60.
921 Wu, Tung-Lin, Arabinda Mishra, Feng Wang, Pai-Feng Yang, John C. Gore, and Li Min Chen. 2016. "Effects of
922 Isoflurane Anesthesia on Resting-state fMRI Signals and Functional Connectivity within Primary
923 Somatosensory Cortex of Monkeys." *Brain and Behavior* 6 (12): e00591.
924 Yu, Xin, Seungsoo Chung, Der-Yow Chen, Shumin Wang, Stephen J. Dodd, Judith R. Walters, John T. R. Isaac,
925 and Alan P. Koretsky. 2012. "Thalamocortical Inputs Show Post-Critical-Period Plasticity." *Neuron* 74 (4):
926 731–42.
927 Yu, Xin, Shumin Wang, Der-Yow Chen, Stephen Dodd, Artem Goloshevsky, and Alan P. Koretsky. 2010. "3D
928 Mapping of Somatotopic Reorganization with Small Animal Functional MRI." *NeuroImage* 49 (2): 1667–76.
929 Zhang, Xian, Xu An, Hanxiao Liu, Jing Peng, Shanshan Cai, Wei Wang, Da-Ting Lin, and Yupeng Yang. 2015.
930 "The Topographical Arrangement of Cutoff Spatial Frequencies across Lower and Upper Visual Fields in
931 Mouse V1." *Scientific Reports* 5 (January): 7734.
932 Zhou, J., S. Clavagnier, and R. F. Hess. 2013. "Short-Term Monocular Deprivation Strengthens the Patched Eye's
933 Contribution to Binocular Combination." *Journal of Vision*. https://doi.org/10.1167/13.5.12.
934 Zhou, Jiawei, Daniel H. Baker, Mathieu Simard, Dave Saint-Amour, and Robert F. Hess. 2015. "Short-Term
935 Monocular Patching Boosts the Patched Eye's Response in Visual Cortex." *Restorative Neurology and*
936 *Neuroscience* 33 (3): 381–87.
937 Zhuang, Jun, Lydia Ng, Derric Williams, Matthew Valley, Yang Li, Marina Garrett, and Jack Waters. 2017. "An
938 Extended Retinotopic Map of Mouse Cortex." *eLife* 6 (January). https://doi.org/10.7554/eLife.18372.

939

# Supplementary Information

1. Robust activation upon complex stimulation
2. Differential BOLD responses to the SF tuning stimulus between DR and HC
3. Correlation between the difference of estimated pRFs position and distance between voxels
4. Goodness of Gaussian fits to the SF tuning curves
5. The differences between HC and DR cannot be explained based on different vascular properties.

## 1. Robust activation upon complex stimulation

Figure S1 shows that the retinotopic and SF tuning stimuli elicited reliable and robust BOLD activation throughout the entire visual pathway of HC, i.e. LGN, VC and SC. Figure S1A and E shows the percentage of BOLD signal change (PSC) of the LGN, VC and SC (Figure S1D) averaged across animals, runs and cycles obtained for both types of complex stimuli. The SF tuning response is overall stronger than the response to the retinotopy stimulus, likely driven by the fact that the SF tuning stimulus is observed across the entire field of view and that the contrast of SF tuning stimulus (100%) was double that of the retinotopy stimulus.

The retinotopy stimulus yielded stronger BOLD responses to the vertical movement, i.e. in the second (84-118 TRs) and fourth (192-216 TRs) stimulation blocks, compared to the horizontal movement (in the first (30-54 TRs) and third (138-162 TRs) blocks), likely due to the preference for vertical movements compared to horizontal ones in rats (Dodwell 1961).

In both stimuli, SC has the strongest response, followed by LGN, and VC has the lowest BOLD response amplitude, following the hierarchical preprocessing from early order areas (LGN, SC) to later areas in the processing of visual information (VC). Also, all visual structures show a post-stimulus overshoot, most noticeable in SC.

Importantly, the activation maps show robust responses limited to the areas of the visual pathway. The activation patterns are consistent across scanning sessions, in particular with the retinotopy stimulus, Figure 4 and S3. For the SF tuning stimulus, the responses of LGN and SC are consistent across scanning sessions, however, the VC's response at t=17d and t=27d is absent or highly attenuated when compared to t=0 and t=7d. This suggests an adaptation to these strong stimuli, rather than e.g. loss of sensitivity given that the VC's response to the retinotopy stimulus remains highly robust at all the time points measured.

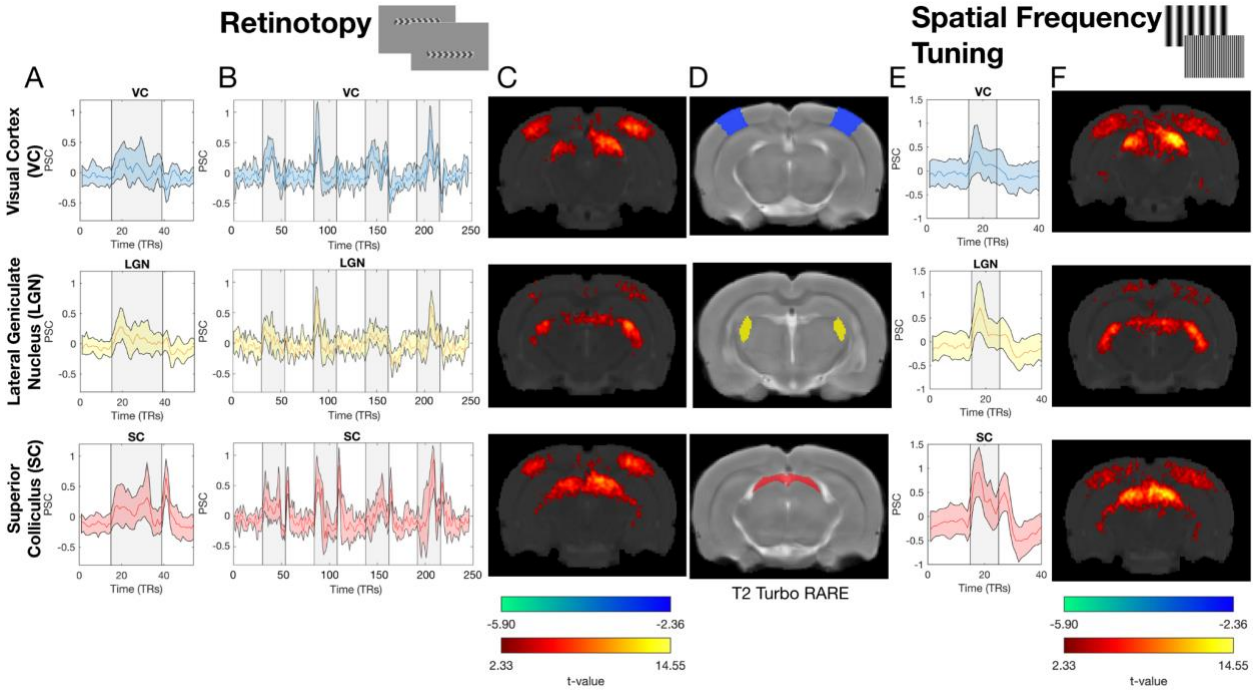


**Figure S1. Retinotopic and SF tuning visual stimuli result in robust BOLD signals confined to the visual pathway in HC at t=0.** A, B and E: Percentage of BOLD signal change (PSC) of the ROIs defined in D averaged across animals, runs (B) and cycles (A, E), upon retinotopic (A, B) and SF tuning (E) visual stimulation. The colored areas correspond to the 95% confidence interval and the gray area to the stimulation period. C and F: GLM functional maps obtained after retinotopic (C) and SF tuning (F) visual stimulation. The maps are FDR corrected using a p-value of 0.001 and minimum cluster size of 20 voxels. D: Anatomical images with the delineation of the ROIs.

# 2. Differential BOLD responses to the SF tuning stimulus between DR and HC

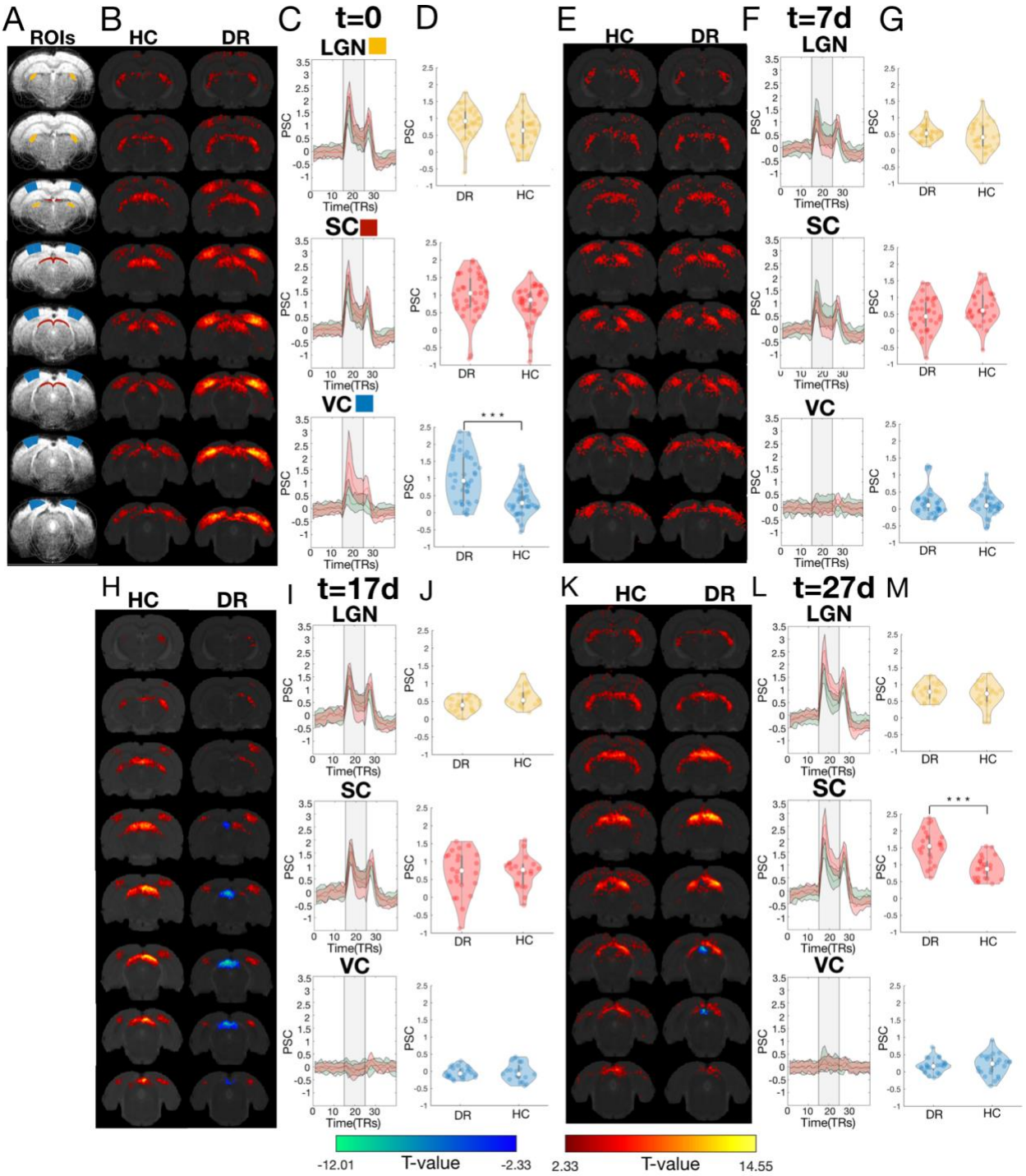


**Figure S2. Differential responses between DR animals and HC driven by the SF tuning stimulus.** A: Raw fMRI images with the ROIs (LGN, SC and VC) overlaid. B, E, H, K: fMRI activation patterns of t-contrast maps obtained for HC and DR animals at t=0, t=7d, t=17d and t=27d, respectively. The GLM maps are FDR corrected using a p-value of 0.001 and minimum cluster size of 20 voxels. C, F, I, L: PSC of the LGN, SC and VC for the HC and DR animals at t=0, t=7d, t=17d and t=27d, respectively. The grey area represents the stimulation period. D,G, J, M: Violin plot of the amplitude of the BOLD response of DR and HC during

the total duration of the activation period obtained with the SF tuning stimulus (right) at t=0, t=7d, t=17d and t=27d, respectively. The white dot represents the mean, and the grey bar represents the 25% and 75% percentiles. The blue, yellow and red colors represent the VC, LGN and SC respectively. The *** represents a p-value<0.001, ** p-value<0.01 and * p-value<0.05.

# 3. Correlation between the difference of estimated pRFs position and distance between voxels

| | HC | | | DR | | |
|---|---|---|---|---|---|---|
| | VC | LGN | SC | VC | LGN | SC |
| t=0 | 0.77 | 0.80 | 0.75 | 0.64 | 0.32 | 0.63 |
| t=7d | 0.77 | 0.76 | 0.74 | 0.78 | 0.32 | 0.72 |
| t=17d | 0.80 | 0.70 | 0.83 | 0.85 | 0.69 | 0.74 |
| t=27d | 0.85 | 0.85 | 0.83 | 0.88 | 0.82 | 0.86 |

**Table S1. Correlation coefficient between the difference of estimated pRFs position and the Dijstra's distance between voxels.**

| | HC | | | DR | | |
|---|---|---|---|---|---|---|
| | VC | LGN | SC | VC | LGN | SC |
| t=0 | 0.000 | 0.001 | 0.000 | 0.005 | 0.286 | 0.001 |
| t=7d | 0.000 | 0.003 | 0.000 | 0.000 | 0.282 | 0.000 |
| t=17d | 0.000 | 0.008 | 0.000 | 0.000 | 0.009 | 0.000 |
| t=27d | 0.000 | 0.000 | 0.000 | 0.000 | 0.001 | 0.000 |

**Table S2. P-values associated with the correlations shown on Table S1.**

# 4. Goodness of Gaussian fits to the SF tuning curves

| Gaussian Fit Tuning Curve $r^2$ | | | | | | | |
|---|---|---|---|---|---|---|---|
| HC | | | | DR | | | |
| 0.61 | 0.35 | 0.73 | 0.85 | 0.81 | 0.45 | 0.00 | 0.66 |
| 0.77 | 0.87 | 0.74 | 0.65 | 0.61 | 0.70 | 0.72 | 0.45 |
| 0.68 | 0.27 | 0.85 | 0.88 | 0.70 | 0.89 | 0.83 | 0.59 |

**Table S3. Pearson's coefficient between the maximum BOLD response to each SF and the Gaussian fit.**

# 5. The differences between HC and DR cannot be explained based on different vascular properties.

In order to verify that the differences in BOLD amplitude and dynamics measured between HC and DR animals are not driven by different vascular properties between the two group of animals and between visual structures, the animals performed a hypercapnia challenge. A total of N = 5 HC (26 runs averaged) and N=5 DR (27 runs averaged) were exposed to 1.5 min normocapnia, 1.5 min hypercapnia and 1.5min normocapnia (Figure 6A). The rise times and signal amplitude nearly identical onsets between DR and HC for the different ROIs (Panels B-G). The mean PSC sinal between DR and HC are highly correlated (VC: $r^2$=0.95 p<0.001; LGN: $r^2$=0.86 p<0.001; SC: $r^2$=0.91 p<0.001 ). In addition a Granger causality test showed that HC hypercapnic response is very useful to predict the DR one (VC: F=10 p-val=0.0017; LGN: F=8.286 p-val=0.0045; SC: F=23 p-val=3.27x$10^{-6}$). This excludes vasculature as the major contributing factor for the different measured timing parameters.In addition the rise times and signal amplitude are nearly identical for all areas, suggesting that the vascular response dynamics becomes dissociated only at later stages.

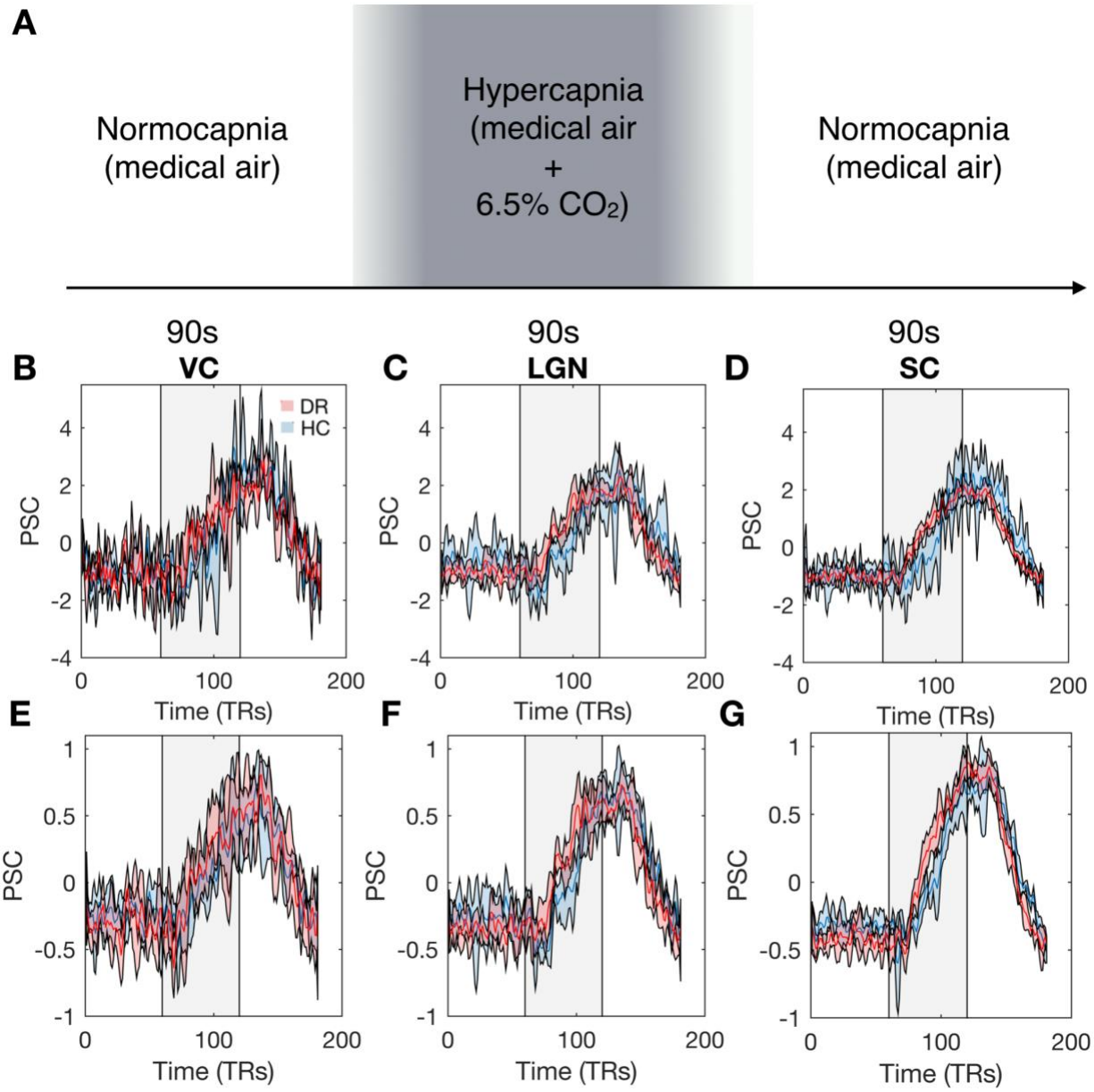


**Figure S3. Hypercapnia experiment testing the dynamics of vascular responses.** A: Hypercapnia paradigm consisted of a manual switch, after 1.5 minutes of medical air, to a hypercapnic state with 6.5% CO2 for 1.5 minutes. This was followed by a manual switch again to medical air for 1.5 minutes. Each run consisted in only one repetition of this block. B, C and D: PSC response profile (mean ± std) obtained for DR (red) anf HC (blue) for different ROIs: VC, LGN and SC, respectively . The shaded grey area indicates the hypercapnic period. E, F and G: Normalized PSC response profile (mean ± std) obtained for DR (red) and HC (blue) for different ROIs: VC, LGN and SC, respectively.